607

ERDA/JPL/954344-76/3

WEB-DENDRITIC RIBBON GROWTH

Annual Report, October 1, 1975—September 31, 1976

R. B. Hilborn, Jr.
J. W. Faust, Jr.

September 31, 1976

Work Performed Under Contract No. NAS-7-100-954344

College of Engineering
South Carolina University
Columbia, South Carolina

ENERGY RESEARCH AND DEVELOPMENT ADMINISTRATION
Division of Solar Energy

DISCLAIMER

NOTICE

Available from the National Technical Information Service, U. S. Department of Commerce, Springfield, Virginia 22161

Price: Paper Copy $5.00 (domestic)
$7.50 (foreign)
Microfiche $3.00 (domestic)
$4.50 (foreign)

Printed in the United States of America
USERDA Technical Information Center, Oak Ridge, Tennessee

ERDA/JPL/954344-76/3
Distribution Category UC-63

Web-Dendritic Ribbon Growth

USC Solar Report No. A-1

Annual Report for Period 10-1-75 to 9-31-76

Authors: R. B. Hilborn, Jr. and J. W. Faust, Jr.

Date of Publication: 9-31-76

JPL Contract No. 954344

Contractor: University of South Carolina
College of Engineering
Columbia, S. C. 29208

This work was performed for the Jet Propulsion Laboratory, California Institute of Technology, under NASA Contract NAS7-100 for the U. S. Energy Research and Development Administration, Division of Solar Energy.

The JPL Low-cost Silicon Solar Array Project is funded by ERDA and forms part of the ERDA Photovoltaic Conversion Program to initiate a major effort toward the development of low-cost solar arrays.

Table of Contents

This report contains information prepared by the University of South Carolina under JPL subcontract. Its content is not necessarily endorsed by the Jet Propulsion Laboratory, California Institute of Technology, National Aeronautics and Space Administration, or the U. S. Energy Research and Development Administration, Division of Solar Energy.

Man-hours and Cost Totals

Previous		Current Year*		Cumulative*	
Man-hours	Cost	Man-hours	Cost	Man-hours	Cost
-----	----	13,356	$176,303	13,356	$176,303

*Figures include baseline cost estimates for month of September, 1976.

Summary

a. Web Growth

The web furnace has been set up, calibrated, and made operational for pulling dendritic-web samples. Considerable work has been completed in the investigation of the effect of changes in the furnace thermal geometry, as accomplished by variations in the number, size, shape, and location of thermal shields, on the growth of dendritic-web. Although shield geometries have been found to optimize button growth and two-dendrite formation no arrangement of the shields has been found suitable to sustain web growth between the two dendrites. Temperature profiles were made by thermocouple probe along the surface of and within the molten Si charge for several of the shield configurations indicating that the proper thermal symmetry for button formation and dendrite growth had been achieved.

Numerous growth runs were made to grow primitive dendrites for use

as the dendritic seed crystals for the web growth. Some preliminary investigations were conducted to try and determine the optimum twin spacing in the dendritic seed crystal for web growth.

b. Web Analysis

Models have been developed and computer programs applied to ascertain the thermal geometries present in the susceptor, crucible melt, meniscus and web. Several thermal geometries have been determined for particular furnace geometries and growth conditions. This information has been studied in conjunction with the experimental growth investigations in order to achieve proper thermal and growth conditions for sustained pulling of two dendrite web ribbon.

A major result of this analysis has been the prediction of an upper limit on the pull rate of approximately 4 cms. per minute with the thermal geometry presented in our furnace. This is predicated on the assumption that a minimum super-cooling temperature of 1407°C must be maintained at the surface of the melt in order to sustain dendritic-web growth. To increase the pull-rate of the web beyond this 4 cm. per minute upper limit will require a furnace geometry which allows increased removal of the latent heat generated at the solid-liquid interface.

c. Web Characterization

The facilities for obtaining the following characterization data have been set-up and made operational:

Twin spacing
Dislocation density
Web geometry, i.e., width, thickness
Resistivity
Majority charge carrier type
Minority carrier lifetime by MOS transient capacitance measurements

Data on twin spacings and number of twin planes in the dendritic seed crystals and resulting web samples has been obtained. Resistivity and majority charge carrier type determinations have been made on a few select web samples. All samples to date have been high resistivity, undoped, p-type.

Interpretation of Results

Web Growth

Insufficient data has been obtained to make conclusions on the optimum twin spacing in the dendrite seeds for dendritic-web growth. It is apparent, however, that poorer button formation and wing development occurs when using seeds with equal spacing between the twin planes.

A large number of growth runs were made utilizing a significant variety of heat shield configurations in order to achieve the proper thermal profile for sustained two dendrite web growth. The best thermal geometry found was achieved with a straight sided susceptor, 4 inches in diameter and 1.25 inches long covered by a single top shield of 0.06 inch thick molybdenum with a standard shaped slot 1.85 inches long and 0.25 inches wide. An alumina disc was used as thermal insulation between the pedestal and susceptor. With this arrangement good button growth and two dendrite formation was consistently achieved. In all cases however, web would form between the two dendrites, but fell out as the ribbon was being pulled. The fall-out occurred typically before the web was pulled through the slot in the top heat shield. These results are interpreted as being due to the top heat shield being too hot and preventing the web from solidifying between the dendrite and the bottom of the button.

Web Analysis

Analysis of the thermal geometry present in the furnace was confirmed by thermal probing of the melt in the crucible with a thermocouple probe. The model being used in the analysis is thus felt to be adequate for use in predicting and confirming the thermal geometry to be expected to result from experimental variations introduced into the furnace while attempting to establish the proper growth conditions for the dendritic-web.

The two-dimensional analysis of the temperatures present in the web and meniscus for various pull rates revealed that the melt temperature, for any given meniscus height, was critically dependent on the pull rate of the web. Thus, if growth conditions require a specific range of temperatures to be maintained in the melt, this would establish the pull rate over which it would be possible to sustain dendritic-web growth. In fact, the minimum temperature that can be maintained in the melt and still sustain growth dictates the maximum pull rate that can be achieved for any specific meniscus height. Under these conditions the maximum meniscus height that can be achieved without thinning the web will give the maximum pull rate. Application of this analysis to our furnace geometry and using the maximum possible meniscus height of 0.76 cm indicated that the maximum pull rate that could be achieved and still sustain web growth was 3.9 cms per minute. A minimum melt temperature of 1407 °C was assumed as the maximum supercooling that could be permitted and still maintain growth.

Web Characterization

The limited characterization data that has been obtained to date indicates that the measurements are valid and that they can be utilized to evaluate the web material grown in our furnace.

Program Efforts

Web Growth

Figure 1 illustrates the Web Growth Furnace which is powered by a 10KW r-f generator operating at 290 khz. The susceptor is fabricated from molybdenum as are the shields and pedestal. The diffuser plate, Figure 2, which is used to diffuse the flow of argon entering the furnace at the bottom, is constructed of stainless steel. A five inch diameter quartz tube, surrounding the susceptor and pedestal and within the water cooled heater coils, is used to contain the inert atmosphere provided by the argon. The dendritic-web is pulled from the quartz crucible, seated in the susceptor, through a slot in the top heat shield to a wind-up reel located above the furnace.

The following check-off list represents the procedural instructions that have been established for the operation of the growth furnace:

Prestart-up

1. Check generator off button on generator.
2. Check filament off button on generator.
3. Check main breaker on rear of generator.

Start-up

Load and assemble the furnace. After this is complete, proceed as follows:

1. Check cooling water on furnace. Turn on both valves - one to furnace and other to generator.
2. Turn on argon flow to 50 cfh.
3. Turn on filament button on generator.

   Note: After the above three items have been accomplished, wait 15 minutes. This will allow the chamber to be purged with argon, and the vacuum tube filaments in the generator to warm up.

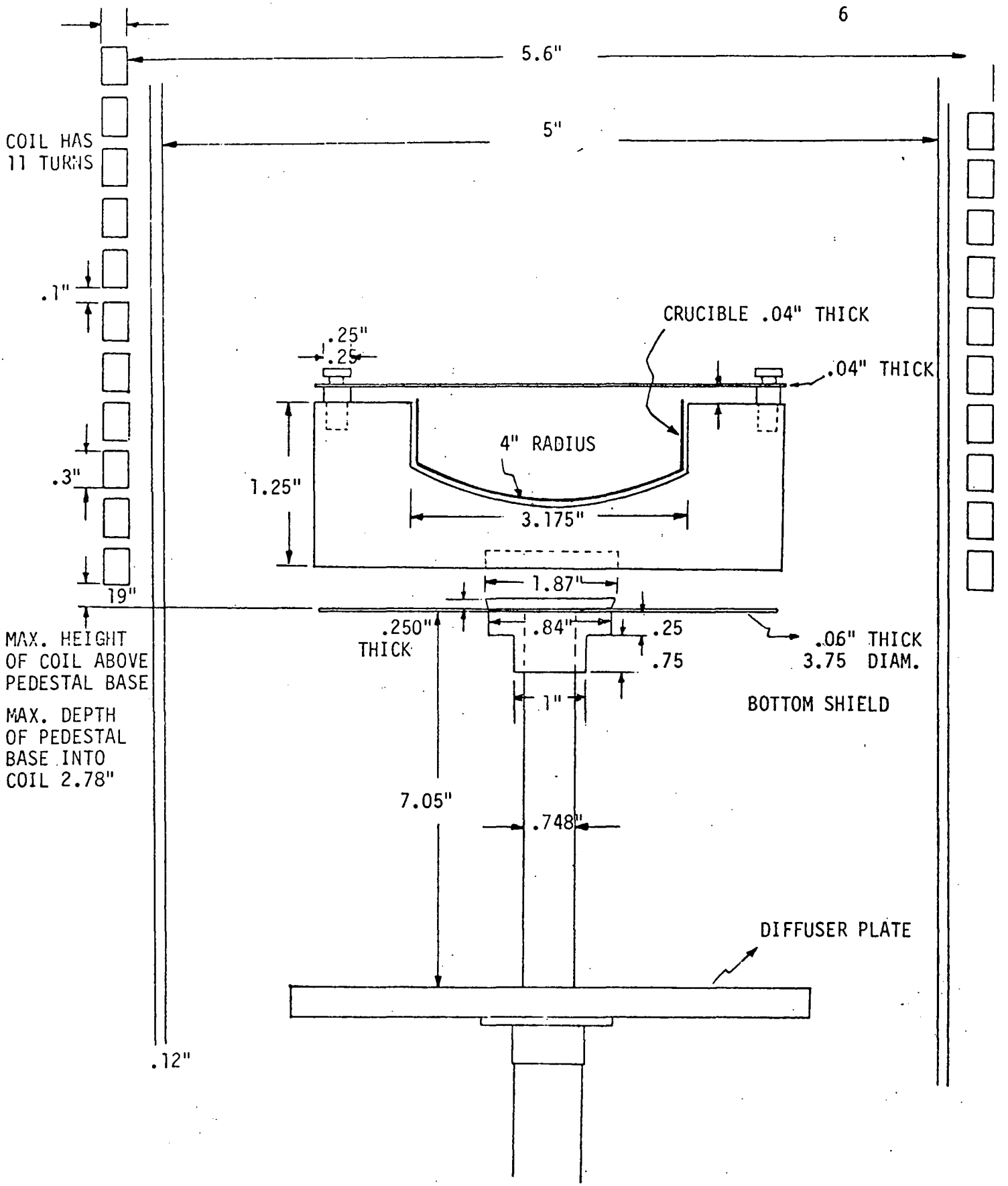

Figure 1. Growth Furnace

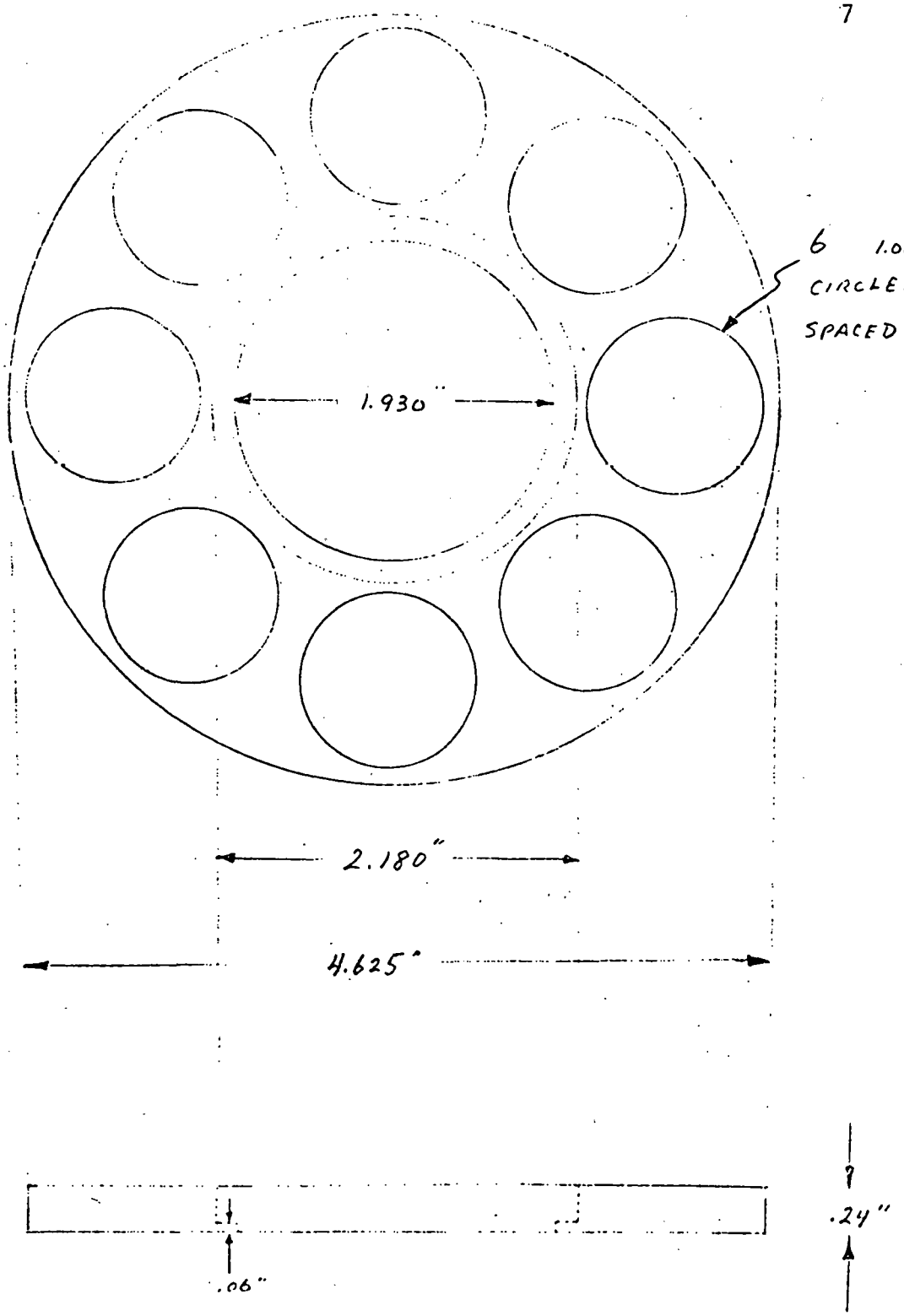

DIFFUSER PLATE

Figure 2

4. Check controller Auto-Manual switch. Put it in manual position and have temperature control on zero.
5. Turn on power button on the generator.

   Caution: Work coil is now HOT!
6. Adjust power to 5 kilovolts until susceptor glows (approximately a minute). Increase power to 6 kilovolts until outgassing stops (approximately 5 minutes). Increase to 8 kilovolts for 2 minutes to let the temperature stabilize. Then increase to 10.5 kilovolts until complete melting is obtained.
7. Decrease argon flow to 35 cfh.
8. Lower temperature to growth value. After the temperature has stabilized it is ready for web growth.

Furnace Shut Down

1. Flip the Auto-Manual switch to Manual.
2. Cut furnace temperature.
3. Turn the generator power button to off.
4. Wait 30 minutes for cool-down and proceed as follows.
5. Turn filament button off.
6. Turn off main breaker.
7. Turn off argon.
8. Turn off water valves.

The following seeding techniques have been followed, with more or less equal success, for initiating the dendritic-web growth:

Seeding Technique #1 ("transient method")

1. Find growth temperature. Growth temperature is taken at

temperature for good button growth, determined by experiment.

2. Raise melt temperature 15 to 20 °C above the growth temperature. Dip seed into melt to melt off end.
3. Reset temperature controller for "growth temperature".
4. As temperature of melt drops, seed is dipped into melt at 5 to 7 °C above the "growth temperature".
5. As melt temperature drops further, button growth begins. When wings form on button, pulling is started at 80 - 100% on the speed controller (this corresponds to 6 to 7 cm per min.).
6. As soon as button starts to rise, decrease pull speed to 10 - 40% (i.e. 2 to 4 cm/min).

Seeding Technique #2 (standard)

1. Find melting point of melt. This is accomplished by dipping a seed into the melt and adjusting the temperature until seed neither melts nor grows. A seed etched to a point gives a more accurate melting point.
2. Set desired ΔT on temperature controller (can be anywhere from 2 - 25 °C. Actually, we are presently using 5 - 20 °C.).
3. As melt temp. drops to new value, button begins to grow. When wings first appear pulling is commenced at 10 - 40% of speed controller (this corresponds to 2 - 4 cm/min.).
4. In this technique the pull speed is not changed unless it is desired to adjust the thickness of the web.

In that the object of our program is to determine the limitation of pull rate and growth width of dendritic-web ribbon, it was deemed essential that our experimental growth runs be conducted using seed dendrites having the optimum twin spacing for the web growth.

The twin spacing for silicon dendrite or web growth had never been optimized. It was deemed in the best interests of the contract to spend some time in growing primitive dendrites, and from these, pulling long dendrites to be used for seeds for web growth.

Primitive dendrites were grown by quickly dipping a seed of silicon into the super cooled melt. Silicon grows rapidly on this "cold" seed, and must be pulled quickly from the melt. The resulting growth mass contains many "growth mistakes" in the form of twins. Only those twin spacings that sustain growth by the twin plane reentrant edge mechanism will result in primitive dendrites protruding from the growth mass. The growth mass with the few protruding primitive dendrites was usually too large to be pulled through the largest opening in our normal heat shield. A special heat shield for use during the primitive dendritic growth was made as shown in Figure 3.

The primitive dendrites were fractured from the growth mass and the twin spacing measured. Longer dendrites for seeds as web growth were pulled from the primitive dendrites for use in studying their behavior to find the optimum spacing.

Runs were made using primitive dendrite seeds having twin spacings of (3 and 2) μm and (8 and 2) μm for comparison with the previously used standard seed having a twin spacing of (0.9 and 1.9) μm. Results to date indicate poorer button formation and wing development with the (3 and 2) μm spacing.

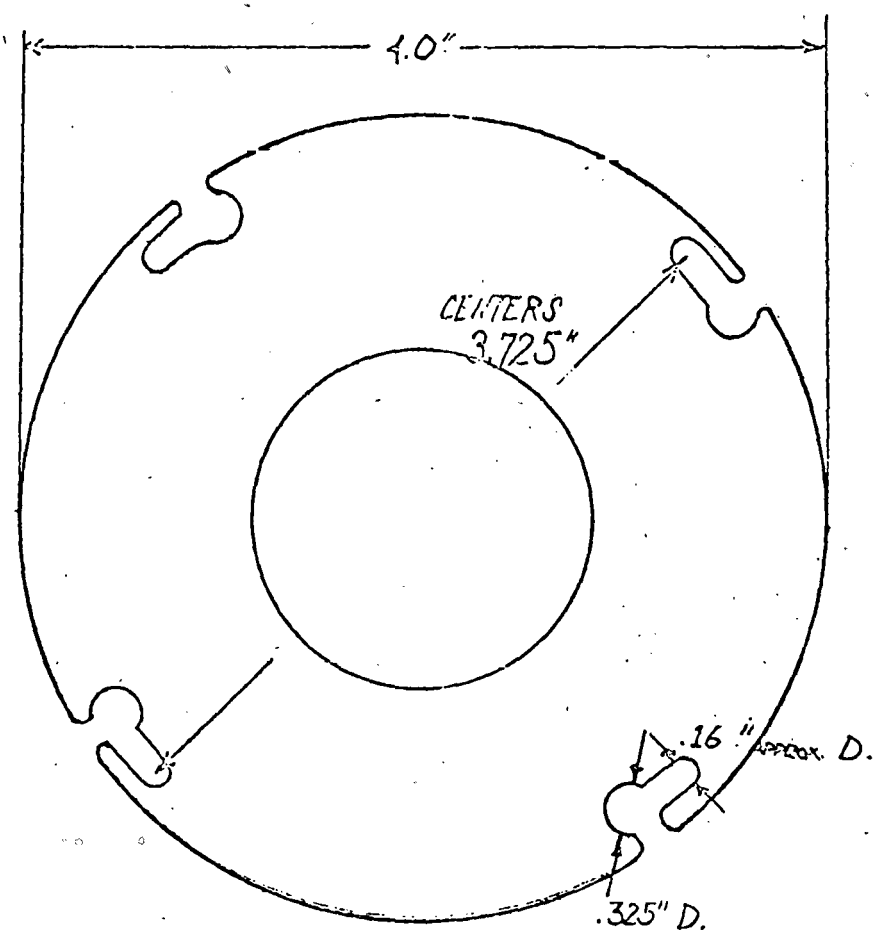

Figure 3. Heat Shield for Pulling Primitive Dendrites

Temperature profiles in the crucible were measured using a Pt-Pt, 10% Rh. thermocouple in a quartz protection tube. These results were then compared with the profile determined by thermal analysis. The results are shown in Figure 4. The experimental points are skewed somewhat to the right because the melt did not achieve a horizontal level in this run. The 4 inch diameter straight sided susceptor with one top shield having an oblong slot 1.85" x 0.25" was used for the run in which these measurements were taken.

The following lists a summary of the results achieved for the different furnace configurations that were tried during the past year in attempts to achieve the proper thermal configuration for two dendrite web growth.

1. Shield #1 (Figure 5)

   4" straight sided susceptor

   Comments:

   Oxide buildup on slot was greater than for larger slot openings.

   Button growth was good. Button aspect ratio: 2/5 average.

2. Shield #1 (Figure 5)

   4" straight sided susceptor

   4.15" Diffuser plate, .25" thick

   Comments:

   The diffuser plate was moved up from the bottom of the furnace chamber to within one inch of the susceptor bottom. This position was inside the coil. The large diameter of this plate caused it to couple too well to the field, robbing power to the susceptor. Subsequently, we were unable to melt any silicon.

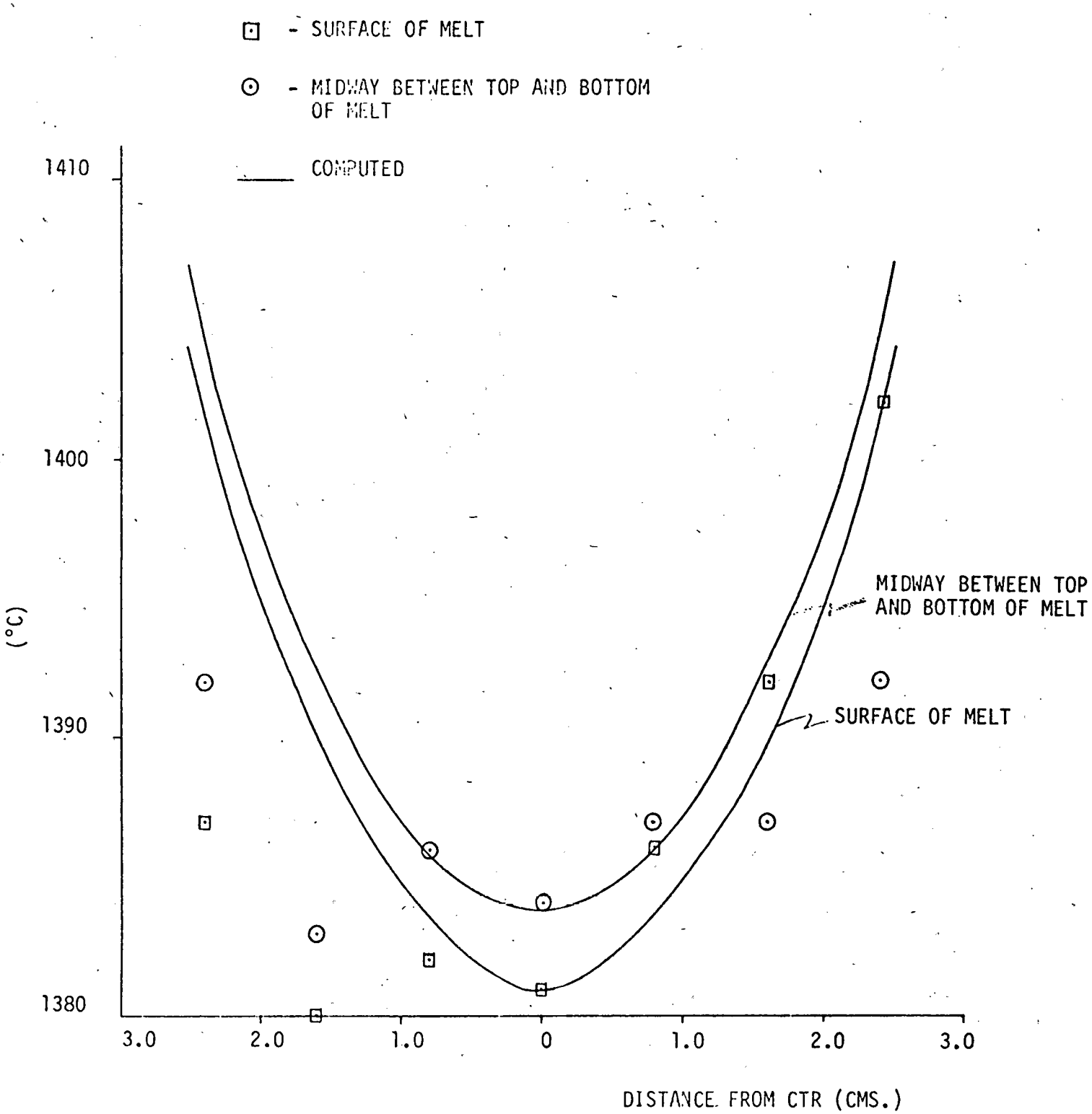

Figure 4. Measured and Computed Temperature Profiles in Crucible

SHIELD # 1

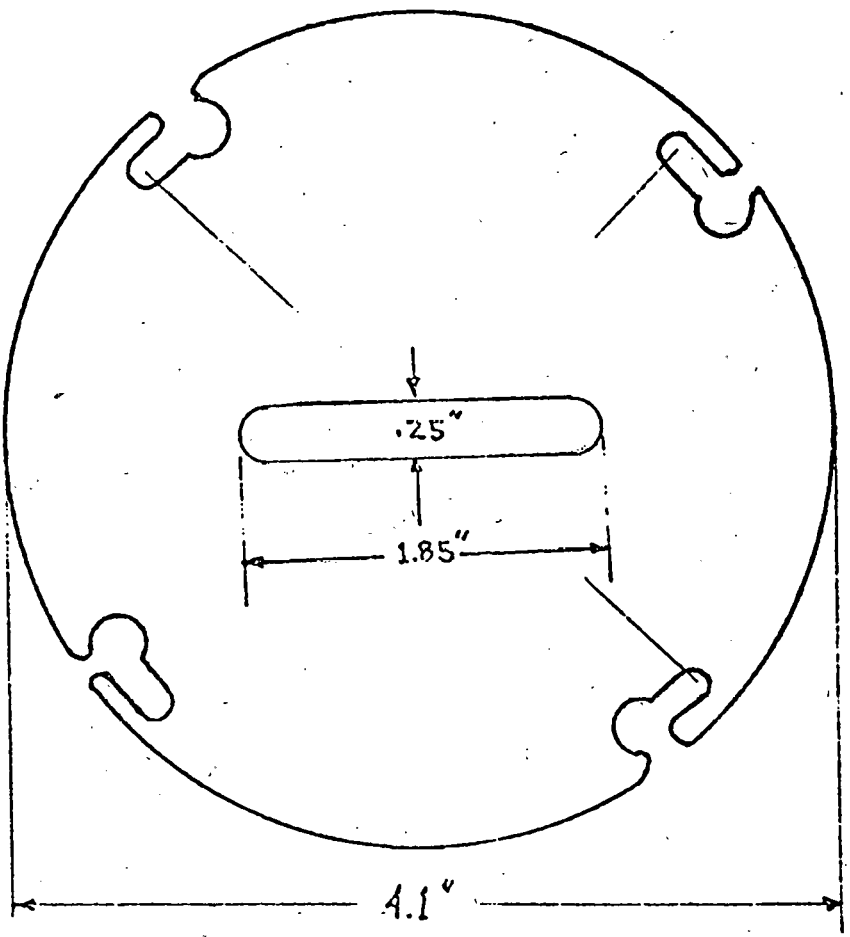

.04 in. MOLY.

Figure 5

3. Shield #1 (Figure 5)

   4" straight sided susceptor

   3.85" x .04" bottom shield

   Comments:

   The bottom thermal shield was placed 1/16" below the susceptor bottom.

   One button was grown with aspect ratio of 1/5, but ice was also observed growing. Three inches of 1 cm. wide multi-dendrite web pulled.

4. Shield #1 (Figure 5)

   4" straight sided susceptor

   3.85" x .04" bottom thermal shield

   Comments:

   Optimum coil setting was not found by the end of the day when a button with dendrites froze to crucible bottom pulling seed free of seed holder.

   Pulled out two pieces: First button was 2/3 aspect ratio with only one wing and three dendrites. Left dendrite joined center leaving 2 dendrite web for 16" when web fell out and dendrites continued. Second piece had a 2/3 aspect ratio button with one wing in the opposite direction from that of the 1st piece. One initial dendrite grew to three dendrites then back to one. A new button was grown on this dendrite which froze to the crucible bottom, pulling the seed free of the holder.

5. Dumbell heat shield #2 mod. 2 (Figure 6)

   4" straight sided susceptor

   3.85" x .04" bottom thermal shield

   .025" Al_2O_3 insulator cut to fit between the pedestal top and susceptor.

   Comments:

   Seven buttons were grown, but nothing was removed. Of the seven, six had wings, and three had 2 dendrites only, but

DUMBELL HEAT SHIELD NO. 2 MOD. 2

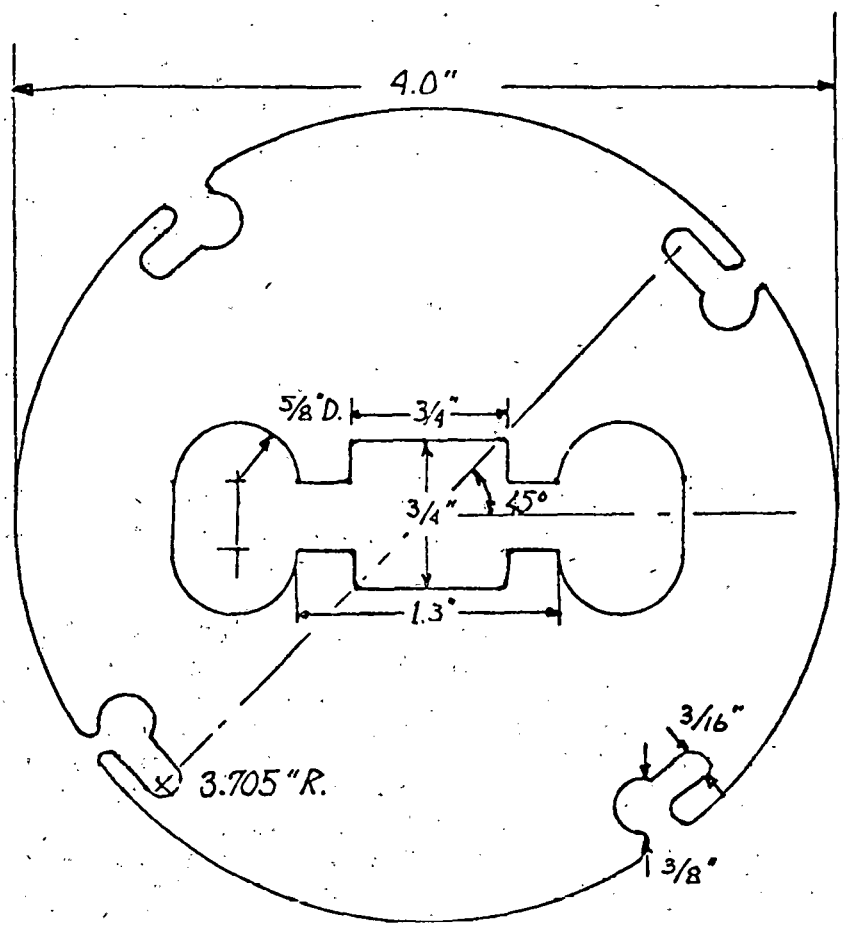

.06 IN. MOLYBDENUM

Figure 6

each case as the pull continued, the web fell out. Average button aspect ratio was 1/2.

6. Shield #7 (Figure 7)

   4" straight sided susceptor

   Alumina insulator between pedestal and susceptor

   Comments:

   Buttons average aspect ratio was 1/3. Wing formation was good. All 2 dendrite web fell out. Some multi-dendrite web held. On the last button, which had 1/2 aspect ratio and one wing with four dendrites, we pulled 19.5 inches of the four dendrite material. This was in 2 pieces of 2 dendrite web with an open space between pieces. This web material was of better thickness and width than any previously grown.

7. Shield #8 (Figure 8)

   4" straight sided susceptor

   Bottom thermal shield

   Alumina susceptor insulator

   Comments:

   The only material removed was a three dendrite piece. The web between the two dendrites farthest apart fell out. The other continued for 16.25". Two other good buttons were grown with two wings and dendrites. The web fell out of both.

8. Shield #7 Mod. #1 (Figure 9)

   4" straight sided susceptor

   Bottom thermal shield

   Alumina susceptor insulator

   Comments:

   Good buttons were almost impossible to grow with this set up. On final button of the day, we got one wing with one dendrite which widened to four. Two dendrites stopped, leaving two dendrite web. We could not keep the web wide, its tendency was to continually narrow. Total length was 70".

SHIELD # 7

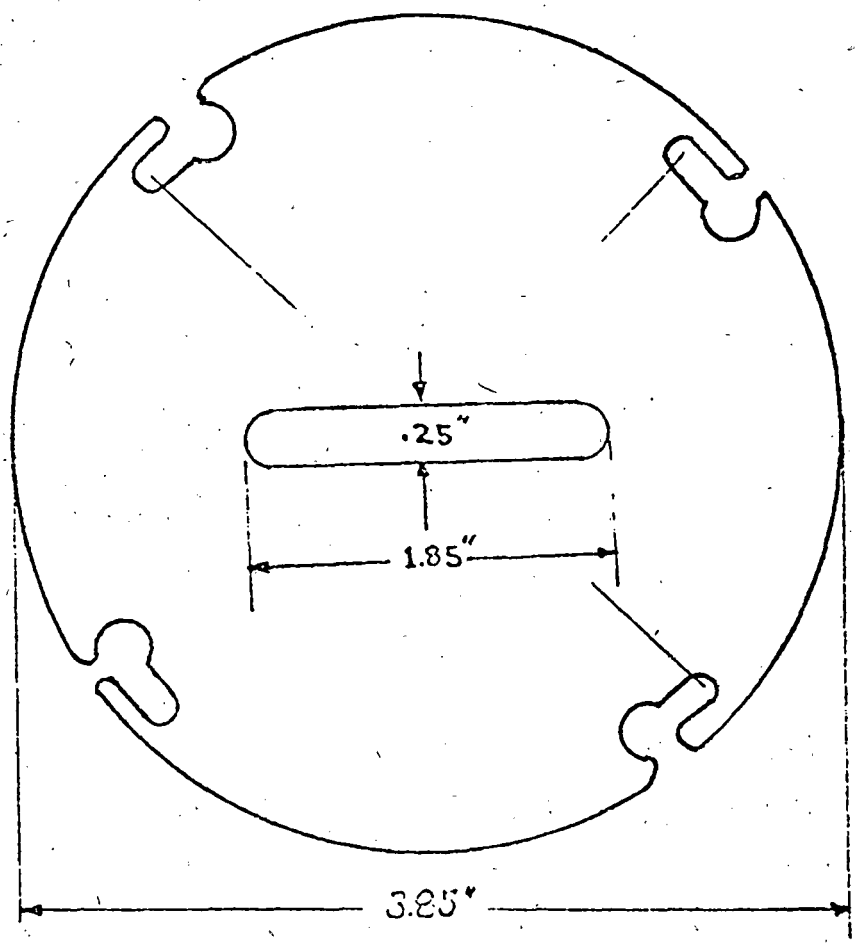

.06" MOLY.

Figure 7

SHIELD # 8

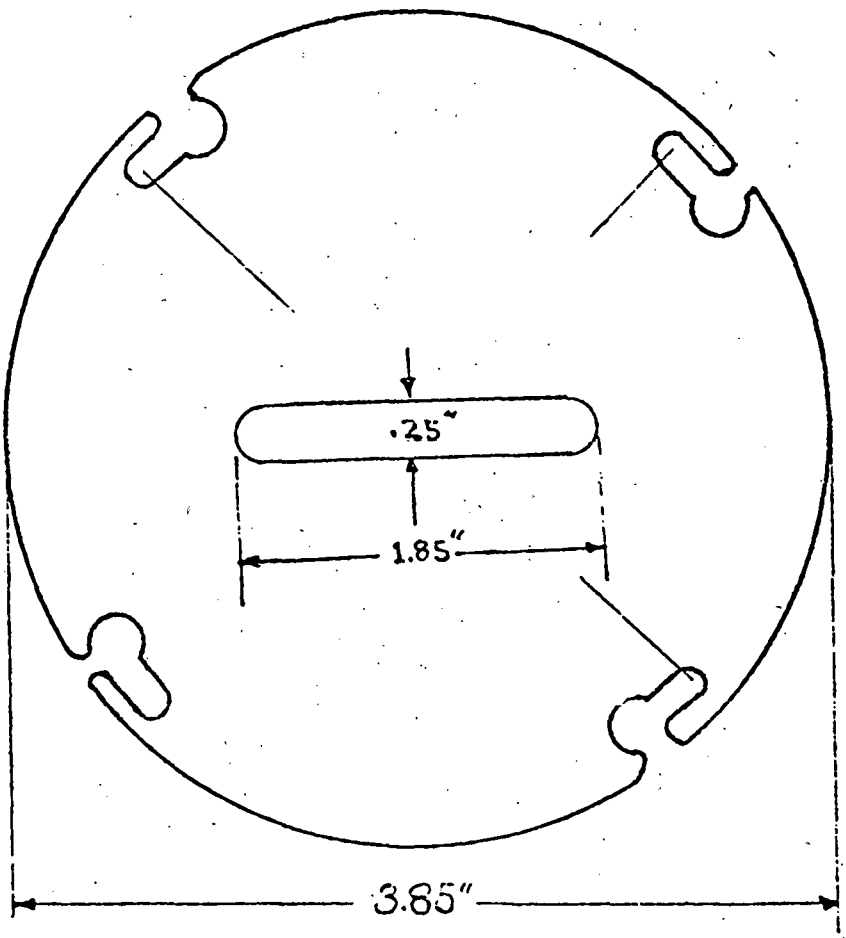

.02" MOLY.

Figure 8

SHIELD #7
MOD# 1

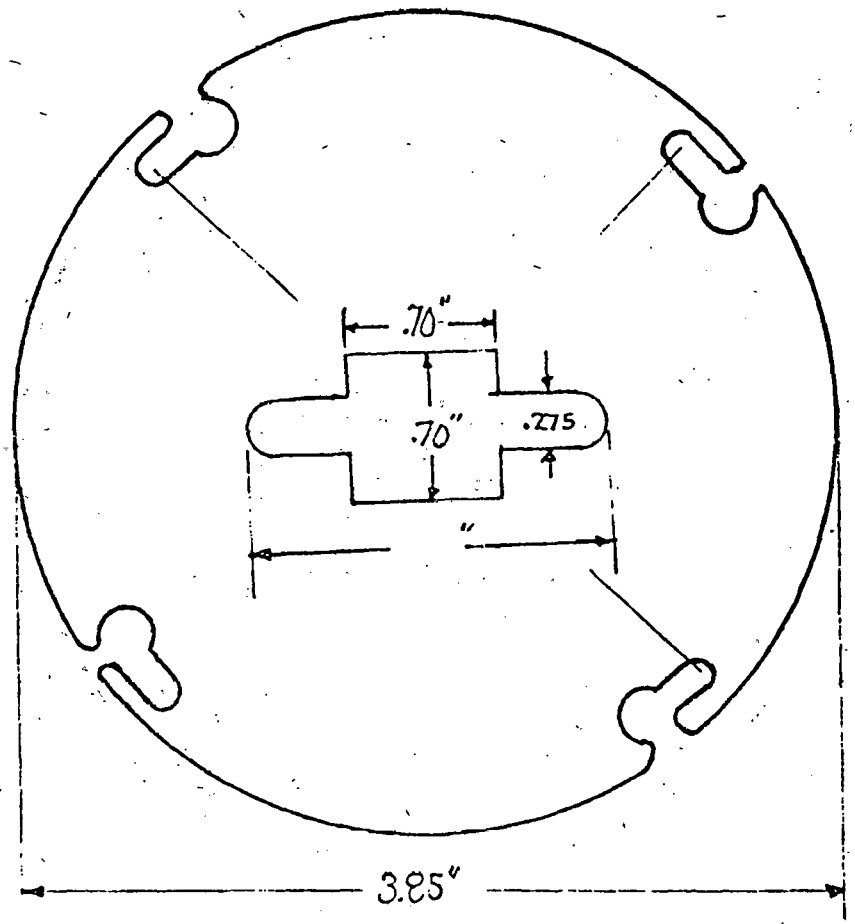

Figure 9

9. Dumbell heat shield #10 (Figure 10)

   4" straight susceptor

   Bottom thermal shield

   Alumina susceptor insulator

   Comments:

   Button growth was poor with large square buttons. When wings were induced, they grew from everywhere.

10. Shield #1 (Figure 5)

    4" straight sided susceptor

    Alumina susceptor insulator

    2 bottom thermal shields separated .25".

    Comments:

    The first thermal shield was against the susceptor support, with the second shield separated from the first by a .25" washer. The shields help cut down the power needed from the generator noticably.

    Oxide build up was so high that later in the day, we could not see the buttons growing.

    Button formation was fair, but no continuous dendrite growth could be achieved.

11. Dumbell shield #1 near the melt (Figure 11)

    Dumbell shield #2 mod. #2 on top of susceptor pins (tantalum) (Figure 4)

    2 bottom thermal shields

    4" straight sided susceptor

    Alumina susceptor insulator

    Comments:

    No good buttons were grown. Buttons usually had no wings. Some buttons froze in the melt before wings could form.

12. 2 top shields dumbell #2 mod. #2 over shield #2 (Figures 6 and 12)

    2 lower termal shields

    4" straight sided susceptor

    Alumina susceptor insulator

SHIELD # 10

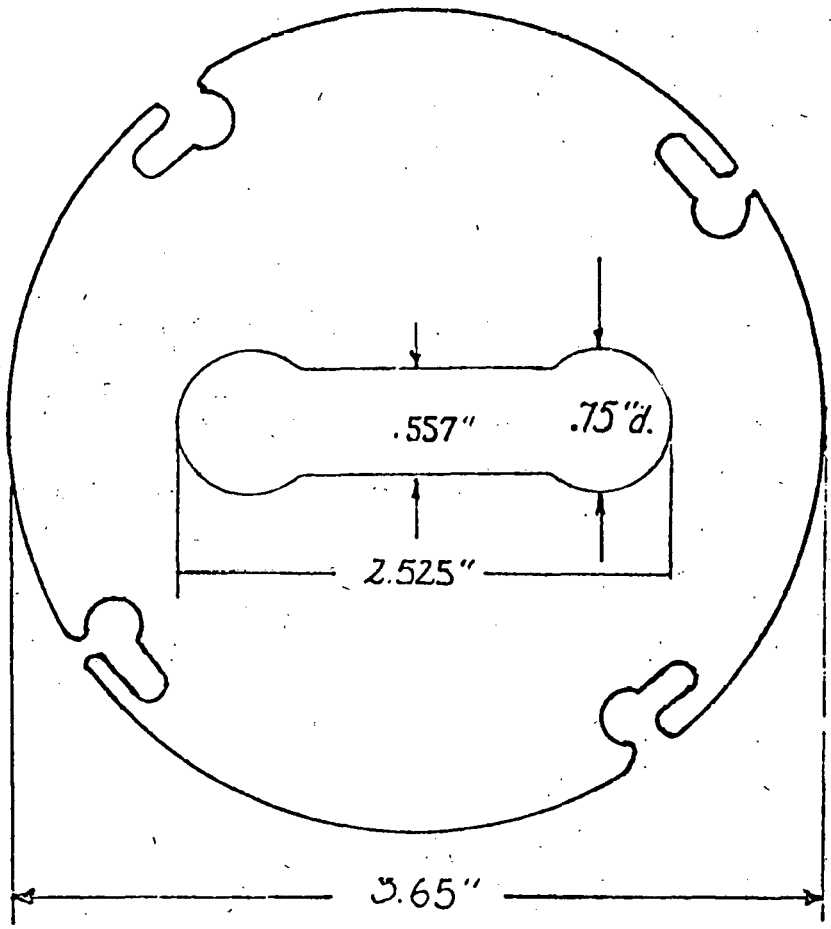

.06" MOLY.

Figure 10

DUMBELL HEAT SHIELD NO. 1

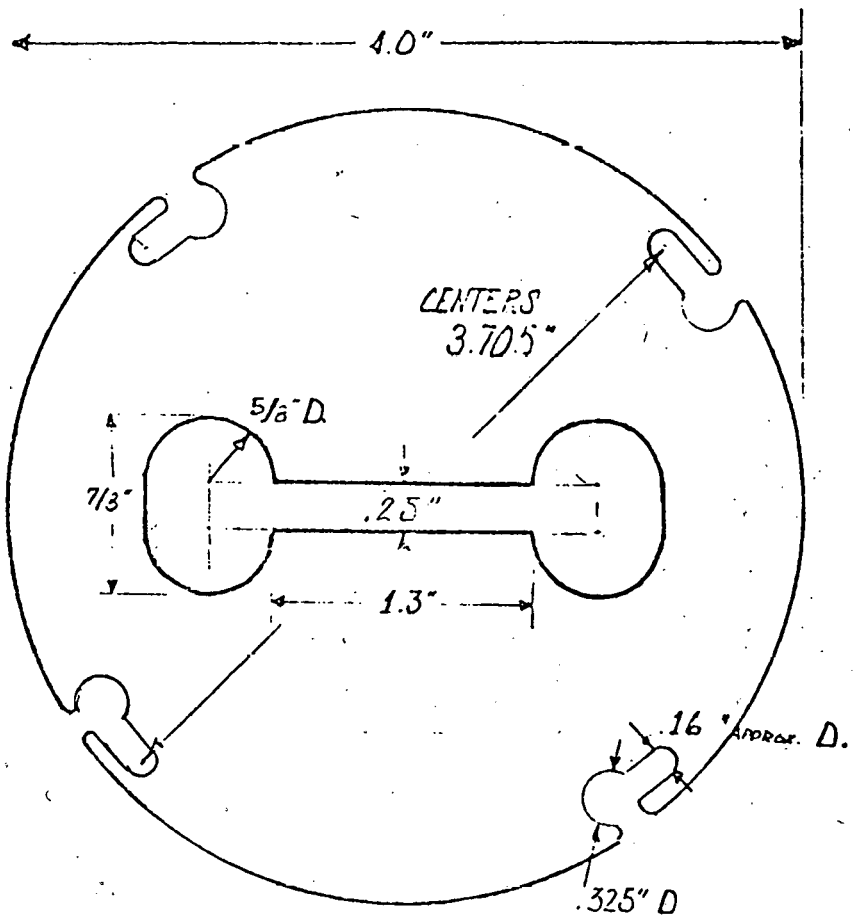

Figure 11

SHIELD # 2

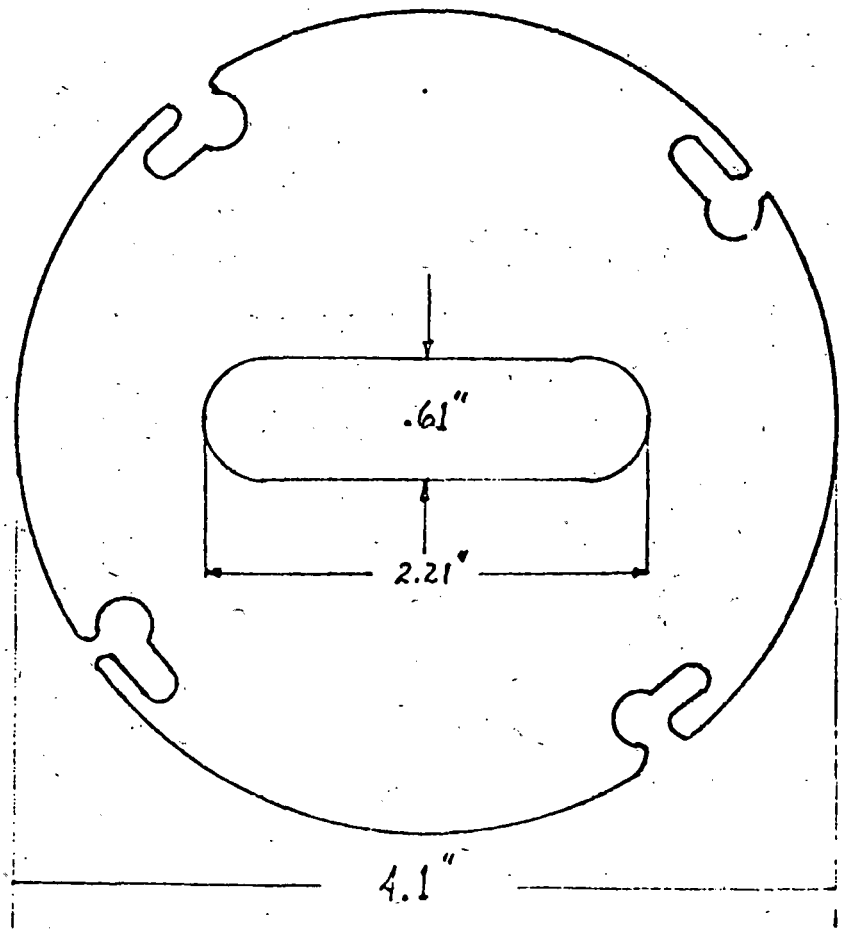

Figure 12

Comments:

Buttons were not very well defined. The corners and sides were rounded somewhat. There were two occasions when the button grew two wings and dendrite, still the web fell out.

Two pieces of material were removed. First button was 2/3 aspect ratio with one wing and 3 dendrites. After one inch, one dendrite stopped. We obtained five more inches of thin two dendrite web. Second button was 1/2 aspect ratio with 2 wings and 4 dendrites. After 5" of 4 dendrite web, 3 stopped, 1 continued for 9".

13. A 2.63" dia. x 2.5" height susceptor was tried. We could not force the generator to melt the silicon charge.

14. 4" straight sided susceptor

2 top shields dumbell #2 (both)(Figure 13)

2 shields bottom

Alumina susceptor insulator

Comments:

Buttons were ill-defined, usually with 3 wings. We were able to remove 2 pieces. 3 other times 2 dendrite web fell out. First piece removed was initally 2 dendrites (very close on small button) but picked up a third dendrite. 3" of 1/4" web and 8" of 3 dendrite material made up this sample. Piece 2 started but with a small 1/1 aspect ratio button 2 wings and 2 dendrites very close together. 2 more dendrites started immediately giving 11.5" of 4 dendrite web.

15. 4" straight sided susceptor

2 top shields, dumbell #2 (both) (Figure 13)

2 shields bottom

Alumina susceptor insulator

Comments:

Button growth fair. Wing formation was good. We grew 3 buttons with 1 wing, 3 with 2 wings, and 1 with no wings. On all 3, 2 winged buttons web fell free of the dendrites at the heat shield.

DUMBELL HEAT SHIELD NO. 2

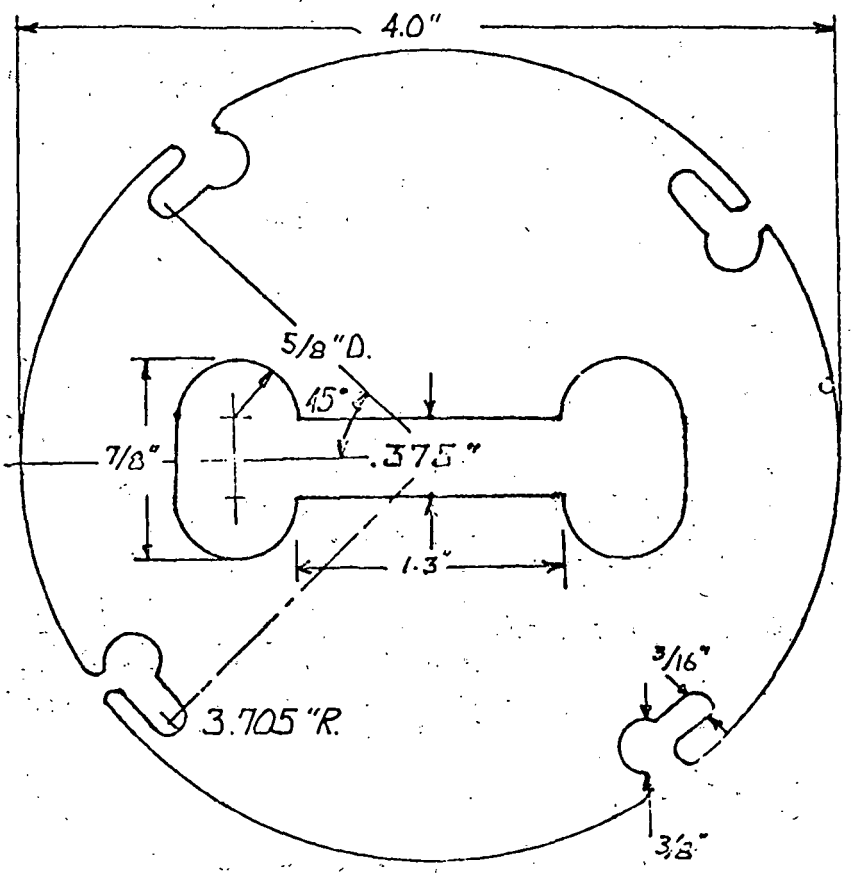

.06 IN. MOLYBDENUM

Figure 13

16. 4" straight sided susceptor

Top shield (one) dumbell #2 (Figure 13)

One bottom shield

Alumina susceptor insulator

Comments:

164 grams of silicon were used today rather than the normal 100 grams. The heat shield was suspended (from outside) directly over the susceptor until the silicon melted. It was then lowered directly on the lip of the crucible so as to get the shield as close to the silicon as possible.

We grew 14 buttons, 4 with one wing, 10 with no wings. Most all of these buttons were abnormal. There was no continuous growth.

17. 4" lipped susceptor

Shield #1 (Figure 5)

One bottom shield

Alumina susceptor insulator

Comments:

Button growth and aspect ratio was very good. Some buttons were as long as 1/4 aspect ratio. Bottom temperature of the melt was too cold though,causing most buttons to freeze to the crucible bottom. 120 grams of silicon were used today. One piece of multidendrite material was grown. The button was 1/3 aspect ratio with two wings and 3 dendrites. There was one extra wing which grew from the growing dendrites. This looked like an arm going out and up from the central core.

18. 4" lipped susceptor

Shield #1 (Figure 5)

One bottom thermal shield which was only 3 1/8" dia. x .06" thick

Alumina susceptor insulator

Comments:

All buttons grown were of good aspect ratio with wings, but everyone froze to the bottom of the crucible.

19. 4" straight sided susceptor

Bottom thermal shield

Shield #7 mod #1 (with 2 pieces of moly covering the mod. to simulate #7) (Figures 7 and 9)

Alumina susceptor insulator

Comments:

Buttons for this run were fair. The same problem of web fall out occurred each time two dendrites were pulled from the melt. 15 buttons grown, 3 no wings, 5 one wing, and 7 with 2 wings.

20. 4" straight sided susceptor 2.5" height (previous 4" susceptors were 1.25" height)

Shield #7 mod. #1 (moly. covering modification)(Figures 7 and 9)

Bottom thermal shield

Alumina susceptor insulator

Comment:

This susceptor with its great mass caused the controller to over- and under-shoot its set points by 5 to 7 degrees. Seven buttons were grown, one with no wings, one with 3 wings, and 5 with 2 wings. In almost every case the web fell out at the heat shield.

Web Analysis

(Meniscus geometry)

Analysis. Theoretical studies have been performed to determine the geometry of the meniscus at the liquid-solid interface of the growing web. The meniscus geometry will have an important bearing upon the growth characteristics of the web as well as the temperature gradients at the interface.

A number of simplifying assumptions have been made. Perhaps the most important assumption is that the static or stationary conditions were assumed. That is, the effect of fluid motion due to web growth was neglected. Uniform melt temperature and uniform constitutent concentrations were also assumed in the melt.

The shape of the meniscus is determined for static conditions using the Euler-Laplace equation which relates the pressure difference Δp across the meniscus to its curvature and the interfacial surface tension γ. That is

$$\Delta p = \gamma\left(\frac{1}{r_1} + \frac{1}{r_2}\right) \qquad (1)$$

where r_1 and r_2 are the principal radii of curvature and are defined to be positive when the center of curvature is inside the region of high pressure. In the present study only the web is considered and consequently the meniscus can be considered two-dimensional and in a plane. Therefore, one of the principal radii of curvature, r_2, is infinite and $\frac{1}{r_2} = 0$.

Figure 14 is a cross-section of the web and meniscus. The angle of contact β is the angle between the solid surface and the liquid surface. Experimental measurements by Swartz, Surek, and Chalmers[1] indicate that β is approximately 11°. Angle θ in Figure 14 is the joining angle of the meniscus

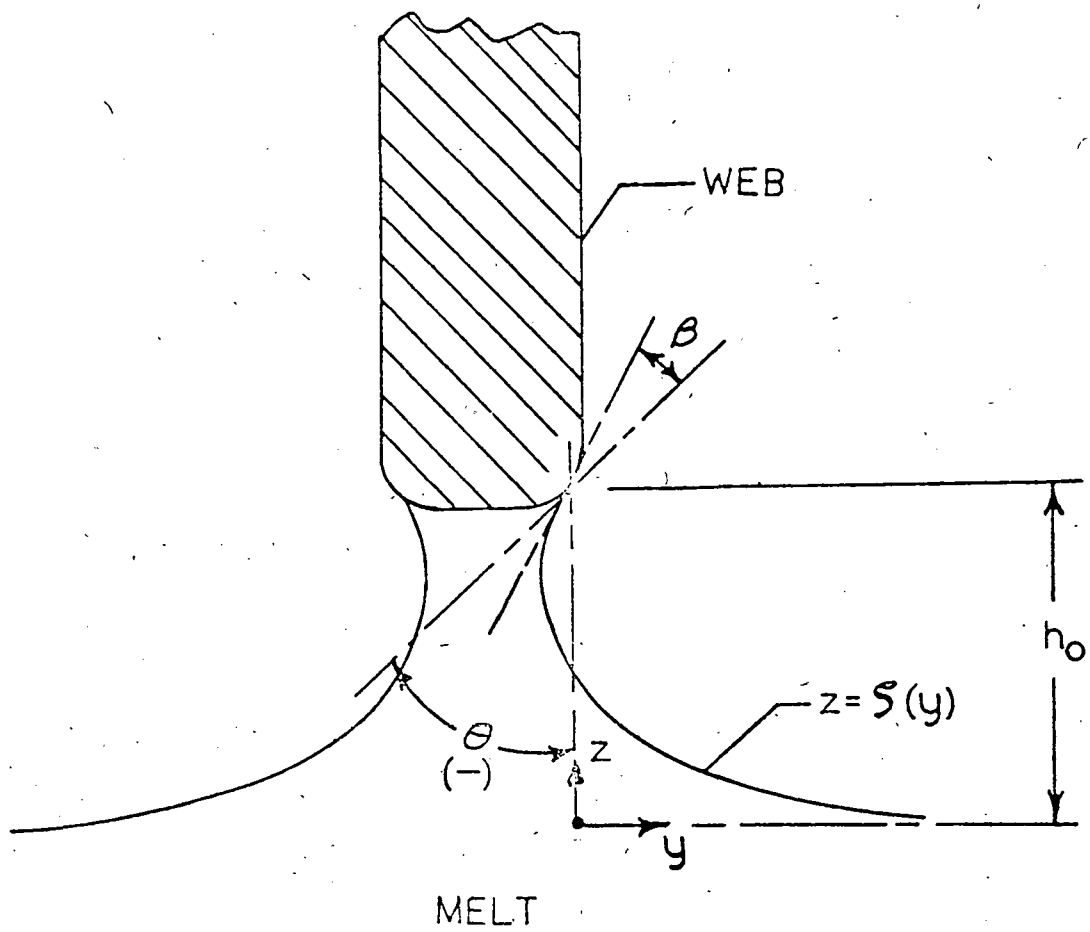

Figure 14. Cross-section of Web and Meniscus. β is contact or wetting angle, θ is joining angle, h_o is height of meniscus at contact, and y and z are horizontal and vertical coordinates.

and is the angle between the meniscus at contact with the solid and the vertical axis. When the top of the meniscus is located on the flat vertical surface of the web, the contact angle β and the joining angle θ are equal. Negative values of θ are measured to the left of the vertical axis and positive values to the right. Thus, the value of θ in Figure 14 would be negative.

Batchelor[2] presents the solution to the Euler-Laplace equation for the two-dimensional plane meniscus. Both the shape of the meniscus and the height can be determined from the results. Gaule and Pastore[3] derived an approximate equation for determining the meniscus height.

Following Batchelor the meniscus height h_o is given by

$$h_o = \sqrt{K\,2(1-\sin\theta)} \tag{2}$$

where

$$K = \sqrt{\frac{\gamma}{\rho g}} \tag{3}$$

and ρ is melt density and g is the acceleration of gravity. The meniscus height h_o is also equal to the height of the interface above the melt level as long as none of the flat vertical surface is immersed in the melt. Further, the shape of the meniscus is given by

$$\frac{y}{K} = \cosh^{-1}\frac{2K}{\zeta} - \cosh^{-1}\frac{2K}{h_o} + \left(4 - \frac{h_o^2}{K^2}\right)^{1/2} - \left(4 - \frac{\zeta^2}{K^2}\right)^{1/2} \tag{4}$$

When y and z are horizontal and vertical cooridinate, $z = \zeta(y)$ is the liquid-gas interface. Note that h_o and ζ are functions of θ but not directly dependent on β. Angles β and θ are related by the geometry of the solid surface at the point of meniscus-solid contact.

Results of Analysis. In Figure 15 the dimensionless term h_o/K given by Equation (2) is shown as a function of θ. The maximum h_o/K is obtained when $\theta = -90°$ and decreases to zero when $\theta = 90°$. The results presented in Figure 15 are independent of the fluid properties and the acceleration of gravity. The terms are included in K which was defined in Equation (3). Taking the values for silicon[1] of $\gamma = 720$ erg/cm^2 and $\rho = 2.49$ gm/cm^3 and the acceleration of gravity of 980 cm/sec^2, it is found that K = 0.543 cm. With the value of K and Figure 15, h can be calculated by multiplying h_o/K by the value of K. For example, Mika and Uelhoff[4] state that for stationary growth (non-increasing or decreasing web thickness), θ must be approximately equal to zero. From Figure 15 the predicted value of h for stationary growth is 0.768 cm.

Figure 16 is a scale drawing of the web and melt cross-section for $\theta = 0°$ and with a web thickness of 0.1 mm. Because of the large surface tension of silicon, a long thin column of melt is present below the web. Menisci geometries were determined using Equation (4) and are shown for various negative values of θ in Figure 17 and positive values in Figure 18. These figures show a section of the meniscus on the right side of the web and the meniscus-solid contact is along the vertical dashed line. Dimensionless coordinates y/K and ζ/K are used so that these curves are general for all fluids. In Figure 17 it is seen that the meniscus is always necked below the liquid-solid interface and the degree of necking increases as θ decreases (more negative). For positive values shown in Figure 18, the menisci are flatter and do not have the neck that occurred with negative values of θ. Note that the height of the meniscus decreases with increasing θ.

Because the webs are very thin, the menisci on the two sides of web can contact for negative values of θ so that the crystal would separate from the melt. This occurrance was not considered previously in studies of

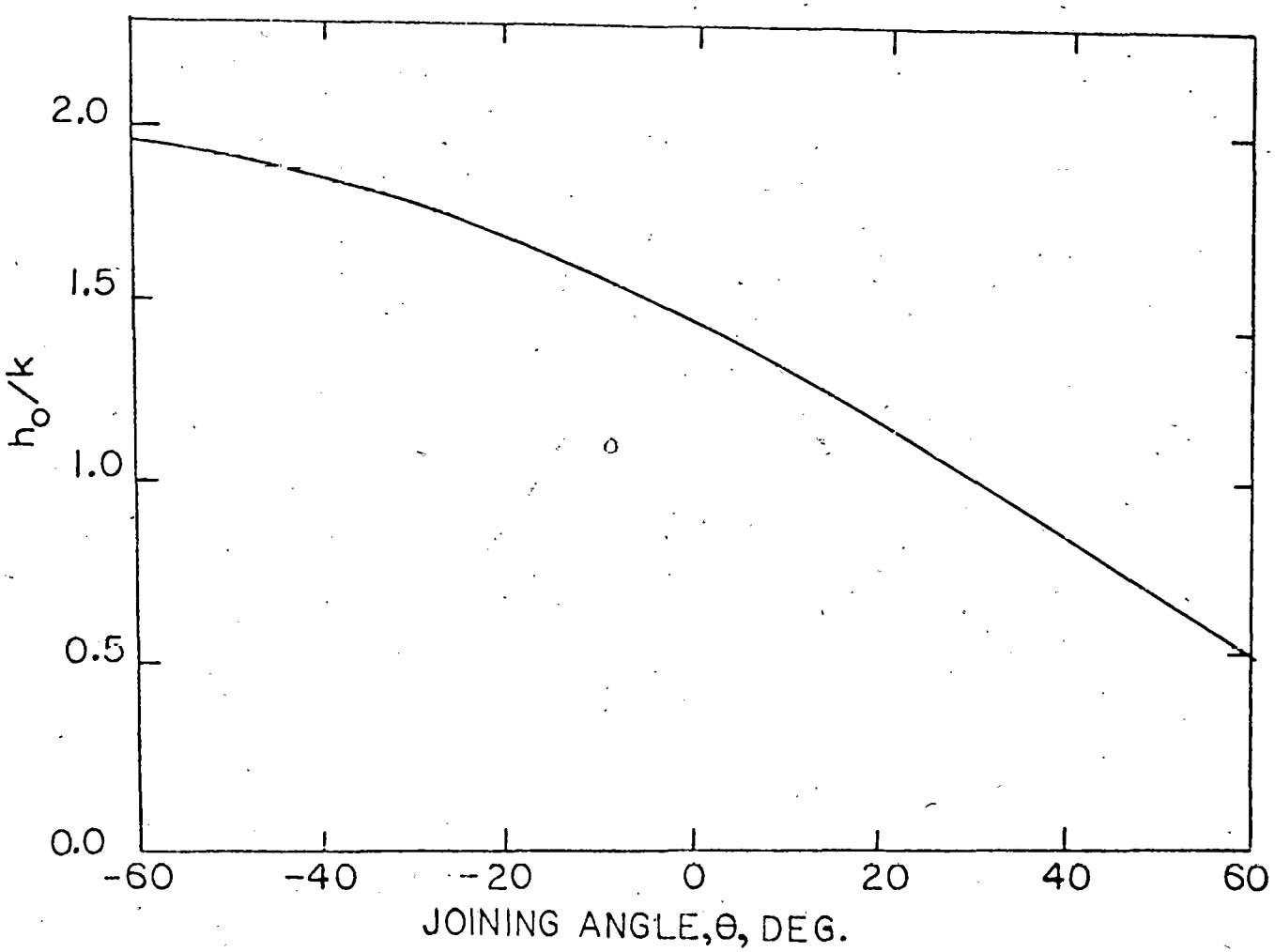

FIGURE 15. Meniscus Dimensionless Height as a Function of Joining Angle θ.

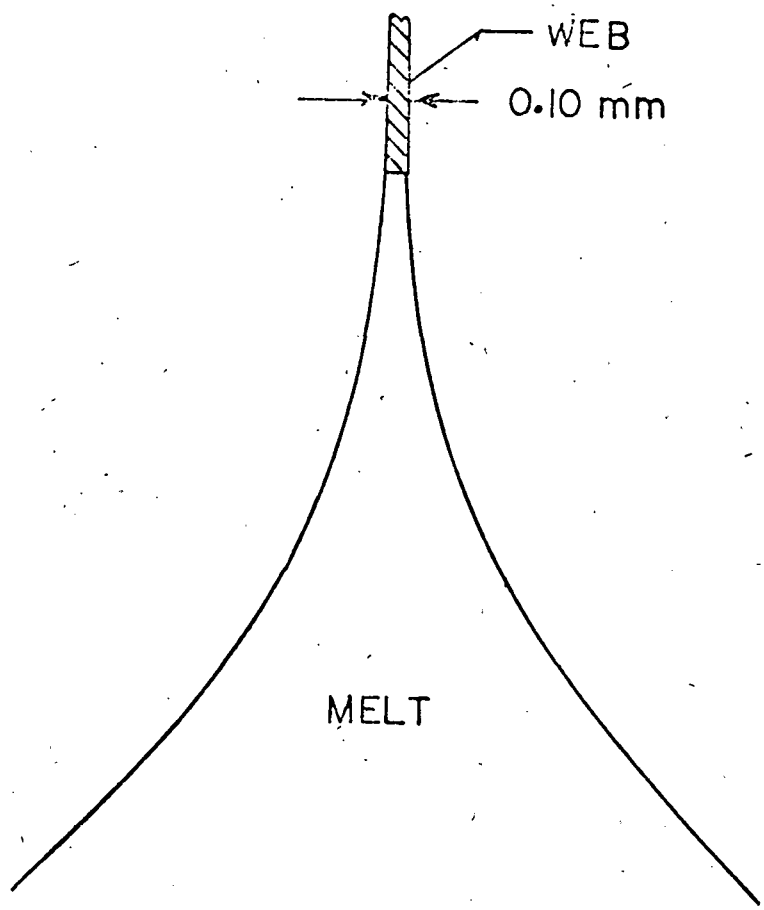

FIGURE 16. Web and Meniscus Cross-section, 0.1 mm Web Thickness and $\theta = 0^{o}$.

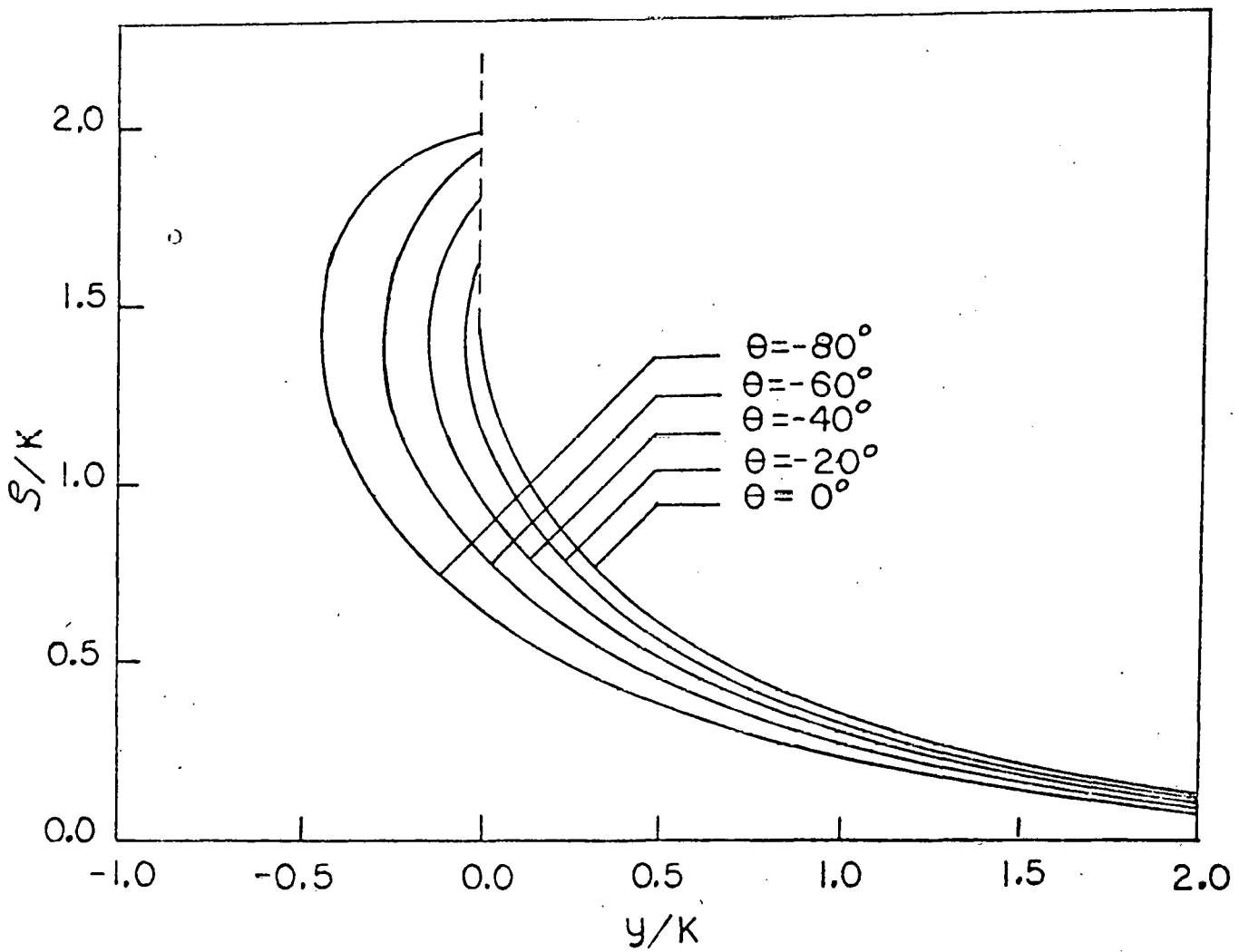

FIGURE 17. Menisci Geometry for Negative Joining Angle θ. ζ/K is plotted as a function of y/K.

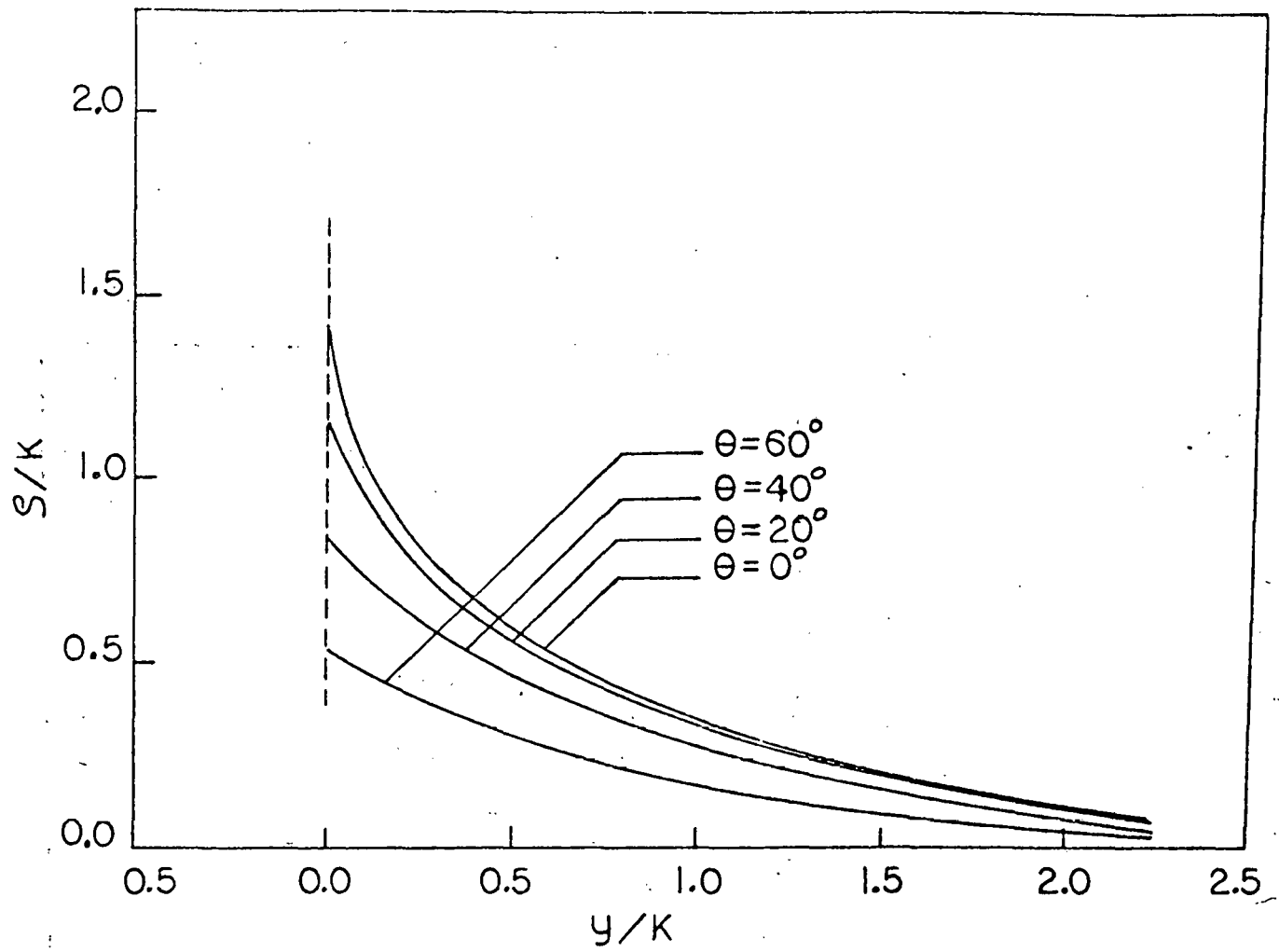

FIGURE 18. Menisci Geometry for Positive Joining Angle θ. ζ/K is plotted as a function of y/K.

Czochralski growth since the diameter of the crystal is usually sufficiently large to prevent separation at the neck. Calculations indicate that the minimum value of θ possible without contact is approximately -10^{o} for silicon with a web thickness of 0.1 mm. The resulting section of the web and melt is shown in Figure 19. A meniscus height of 0.830 cm was determined for this condition using Figure 15 and assuming K = 0.543.

As the liquid-solid interface is lowered, the equilibrium joining angle θ has been shown to increase. As was pointed out earlier by O'Hara and Bennett[5], the web can be caused to extend into the liquid and a region of the flat web will be immersed in the melt. It was pointed out that this may not be a desirable condition since nucleation may occur on the web surface resulting in a widening of the web. As mentioned earlier, when the top of the meniscus is located on the vertical web surface the angles β and θ are equal. Assuming β equal to 11° [1] then we find from Figure 15 that h_o = 0.693 cm. A section of the web and melt for this condition is shown in Figure 20. The height of the meniscus is independent of the position of the end of the web.

To summarize, the studies by Gaule and Pastore[3] and Mika and Uelhoff[4] indicate that θ must be maintained at approximately zero degrees in order to obtain a uniform crystal thickness. It is predicted that the meniscus height for the silicon web would be 0.768 cm. This is also the approximate height of the interface. The magnitude of variation from this height that might be possible and still obtain flat crystals will require a thermal model. However, the results obtained in this study place some limits on the variations. The maximum height is limited by contact of the two menisci which occur at a height of 0.830 cm. Since thickening of the web may occur when the flat vertical {111} surface of the web becomes immersed in the melt, a minimum height of 0.693 cm would be possible without immersion. Further study may determine that the temperature

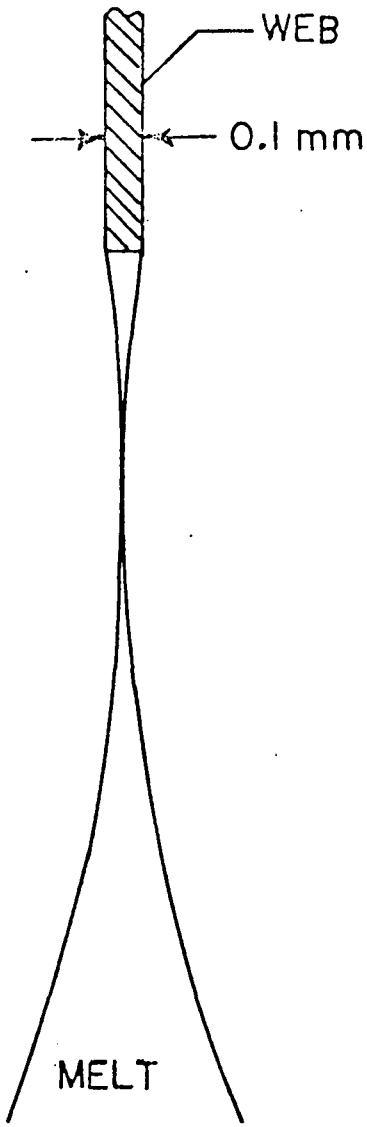

FIGURE 19.Web and Meniscus Cross-section for $\theta = -10^{0}$ and Silicon Melt.

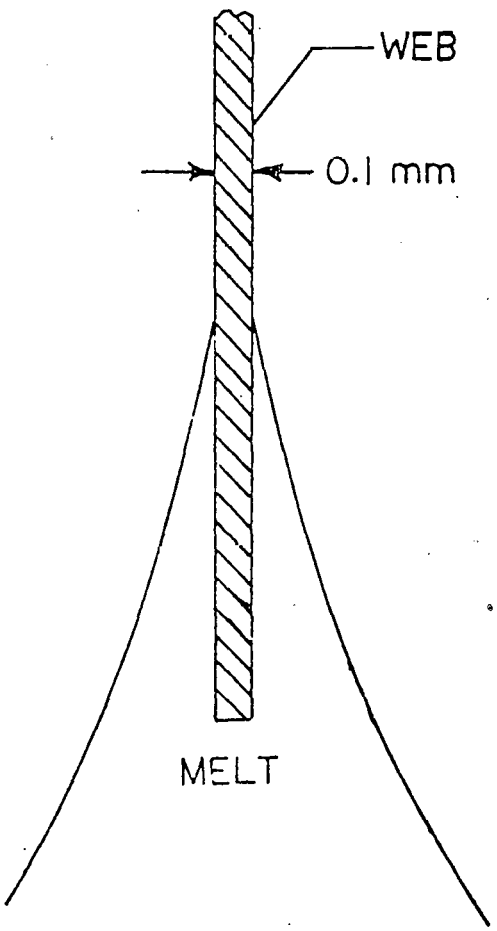

FIGURE 20. Web and Meniscus Cross-section for $\theta = 11^{o}$ and Silicon Melt.

is sufficiently near the melting point that nucleation does not occur and, therefore, the lower limit may be less than the 0.693 cm.

The temperature distribution in the web and meniscus is being investigated with a one-dimensional heat transfer model. Figure 21 shows a cross-section of the web and meniscus. Temperature variations in the z-directions are expected to be large compared to variations across the width and thickness. Heat transfer occurs in the z-direction by thermal conduction and heat convection as a result of pulling the web. Heat exchange between the surface and surroundings is by thermal convection and radiation.

The differential equations for the temperature variation with elevation can be determined by an energy balance on a small elemental volume. The differential equations for the temperature variation in the web and meniscus are respectively,

$$\frac{d^2T}{dz^2} + \frac{\rho_s C_{ps} V}{K_s} \frac{dT}{dz} - \frac{hP}{K_s A_s} (T-T_a) - \frac{P(W-\alpha H)}{K_s A_s} = 0 \qquad (5)$$

and

$$\frac{d^2T}{dz^2} + \left(\frac{1}{A_m} \frac{dA_m}{dz} + \frac{\rho_s C_{pm} A_s V}{K_m A_m} \right) \frac{dT}{dz} - \frac{hP}{K_m A_m} (T-T_a)$$

$$\frac{-P(W-\alpha H)}{K_m A_m} = 0 \qquad (6)$$

where

A - cross-sectional area

c_p - specific heat

H - total irradiance of surface

h - convertive heat transfer coefficient

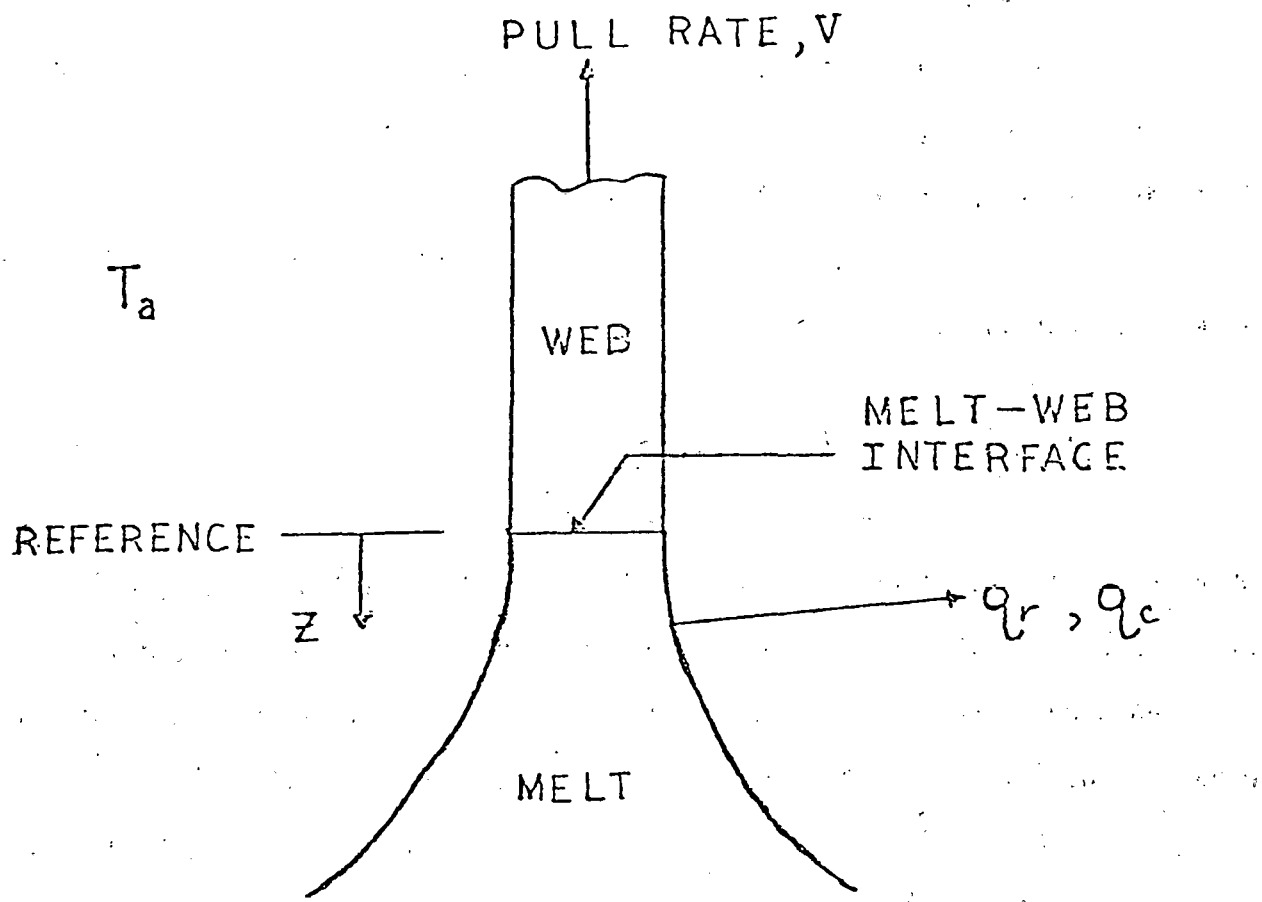

Figure 21. Cross-Section of Web and Meniscus at the Liquid-Solid Interface

K - thermal conductivity

P - perimeter

T - temperature of web or meniscus

T_a - temperature of atmosphere

V - web pull velocity

W - emissive power of surface

z - distance from liquid-solid interface

α - thermal radiation absorptance of surface

ρ - density

Subscripts s and m indicate solid and melt, respectively.

A thermal balance at the liquid-solid interface yields the following interface condition,

$$-K_s A_s \left.\frac{dT}{dz}\right|_s + K_m A_m \left.\frac{dT}{dz}\right|_m + \rho_s A_s V L = 0 \qquad (7)$$

where L is the latent heat of fusion of the silicon and $\left.\frac{dT}{dz}\right|_s$ and $\left.\frac{dT}{dz}\right|_m$ are respectively the temperature gradients in the web and melt at the interface. It is assumed in Equation (7) that the temperature of the solid and liquid are equal at the interface, that is, interface subcooling is negligible.

Because of the complexity of the governing differential equations given by Equations (5) through (7) an analytical solution is not possible. Therefore, numerical solutions are obtained using the computer.

The greatest difficulty in obtaining accurate temperature calculations is predicting the irradiance, H, of the web and meniscus. The term is contained in Equation (5) and (7) and is the thermal radiation received primarily from the lid and silicon melt. The value of H is a function of z since the view factor from the lid and silicon melt varies with position.

The temperature distribution in the silicon web and meniscus is presently being investigated using the CSMP3 model. Figure 22 is some results of that calculation and shows the temperature as a function of distance above the melt surface. The conditions assumed in these calculations are listed in Table 1. In addition to these conditions it was assumed that the joining angle of the meniscus with the solid web is zero degrees. It is seen in Figure 22 that the temperature of the melt is highest in the crucible and decreases approximately 12 °C upon reaching the liquid-solid interface. Due to the latent heat release at the liquid-solid interface, the temperature of the melt remains approximately constant for some distance below the interface. The increased rate of temperature decrease after the liquid-solid interface is primarily due to the lower thermal conductivity of the solid. Radiation heat transfer occurs between web, lid, and silicon melt. This heat interchange has been included in the model. Table 1 lists the lid and melt temperatures assumed in the calculations.

Parametric studies were made of the temperature distribution in the meniscus to determine the effect of crystal pull rate, web thickness, thermal shield geometry, and thermal shield temperature on the growth characteristics at a meniscus joining angle of 0°.

Figure 23 shows the temperature distribution in the web as a function of distance from the liquid-solid interface for a 0.1 mm thick web for pull rates of 1 cm/min and 5 cm/min. The more rapid decrease in web temperature occuring at approximately 0.7 cm from the interface is due to thermal radiation effects of the thermal shield. Below the thermal shield the web receives thermal radiation from the melt and bottom of the thermal shield. For regions of the web above the thermal shield, radiation is received by the upper surface of the thermal shield and surrounding furnace surfaces which are much

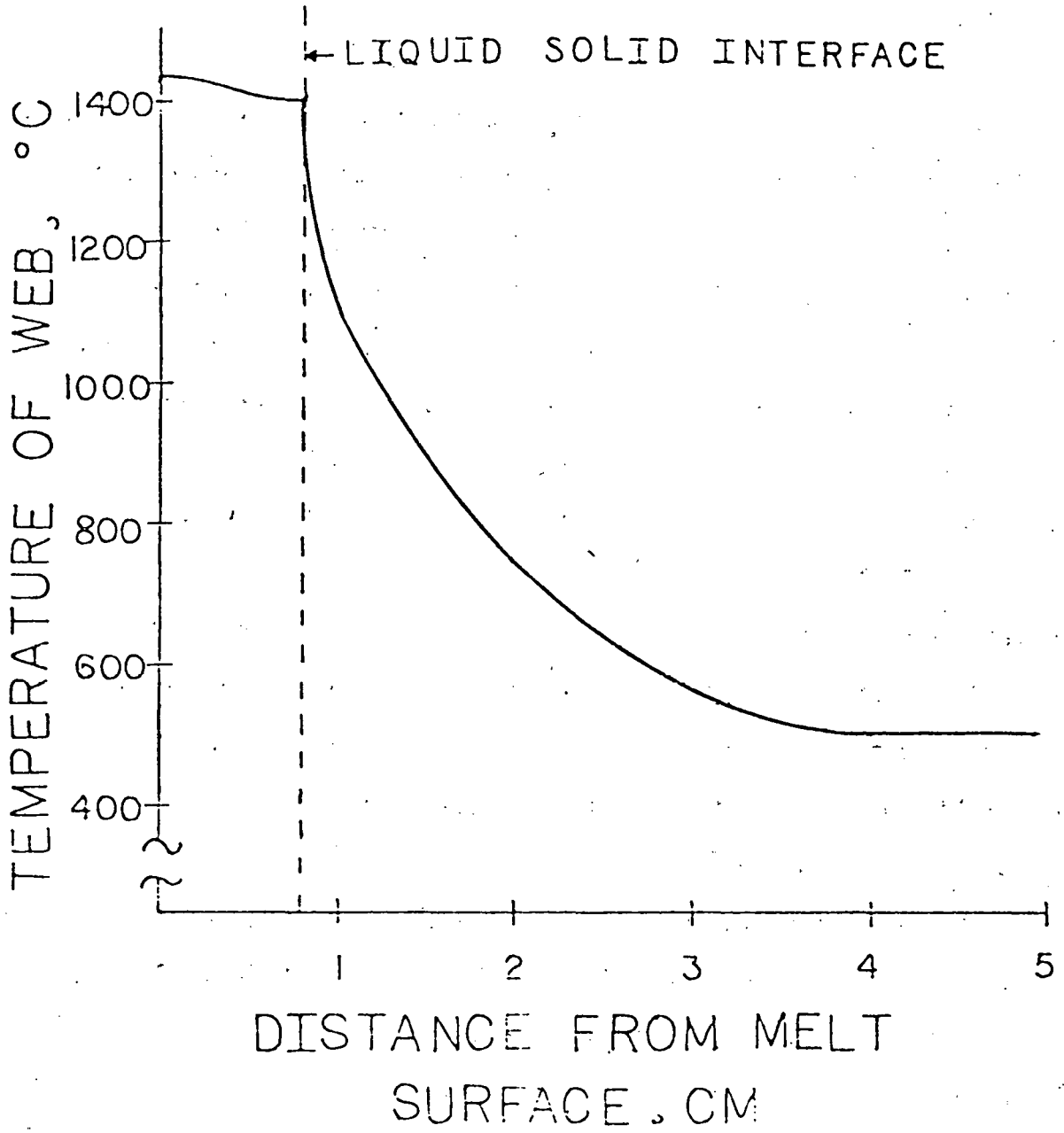

Figure 22 Temperature of Meniscus and Web as a Function of Distance from Melt Surface. Growth Parameters are listed in Table 1.

PHYSICAL CONSTANTS

PARAMETER	VALUE
PULL RATE	5 cm/min
WEB THICKNESS	4 mils
TEMPERATURES:	
INTERFACE	1412°c
LID	≈1300°c
EMISSIVITY:	
SILICON SOLID	.3
SILICON MELT	.22
MOLYBDENUM	.37
CONDUCTIVITY:	
SILICON SOLID	.22 w/cm°k
SILICON MELT	.6 w/cm°k
SPECIFIC HEAT	.162 $\frac{cal}{gm\text{-}^{\circ}c}$
LATENT HEAT OF FUSSION	430 cal/gm
DENSITY:	
SILICON SOLID	2.3 gm/cm^3
SILICON MELT	2.53 gm/cm^3

Table 1 Growth Parameters for Meniscus and Web Temperatures Shown in Figure 8.

Graph of Temperature Distribution in Web at: (1) 1 cm/min
(2) 5 cm/min

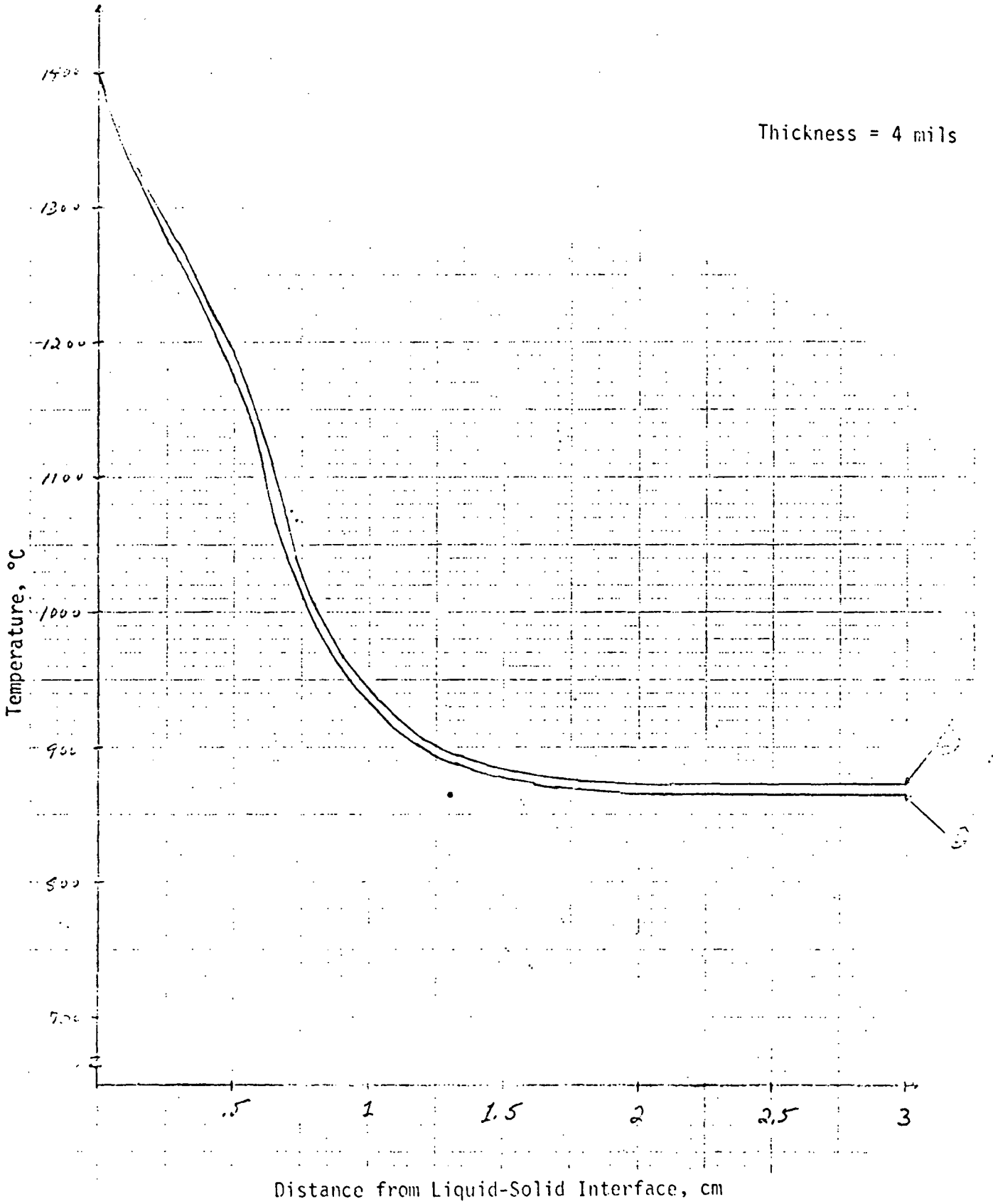

Figure 23. Temperature of web as a function of distance from the liquid-solid interface.

cooler. Consequently, the thermal radiation heat transfer is greatly diminished as the web passes through the slot in the thermal shield. The temperature becomes reasonably steady above the thermal shield since thermal radiation intensity is relatively constant.

It is seen in Figure 23 that the pull rate has a small effect on the temperature of the web. However, the temperature of the melt in the meniscus is affected appreciably by the pull rate. Figure 24 shows the melt temperature as a function of position above the melt surface of the crucible for pull rates of 1,2,3,4, and 5 cm/min. It is seen that the meniscus melt temperature varies considerably with pull rate. The temperature of the melt in the meniscus at the level of the melt is expected to closely approximate that of the region surrounding the growth region including the region of the growing dendrites. Therefore, only the pull rate for which the surface temperature of the melt has approximately 5° supercooling appears physically realizable. Figure 25 shows the melt surface temperature as a function of pull rate. It is seen that melt temperature of 1407° is obtained at a pull rate of 3.9 cm/min. Either higher or lower rates could conceivably result in failure of the web growth. Consequently, it appears that accurate control of the growth rate is required.

The results presented are applicable to the present furnace thermal geometry being used and the pull rate is within the experimental range. It is expected that the thermal geometry will have considerable effect on pull rate. The thermal shield temperature, for example, will have considerable effect on the pull rate. The thermal shield temperature was assumed to be 1260° and was determined from the thermal model of the melt, susceptor, crucible, and thermal shield. A higher temperature will reduce the pull rate.

Graph of Temperature Distribution
In Meniscus

at: (1) 1 cm/min
(2) 2 cm/min
(3) 3 cm/min
(4) 4 cm/min
(5) 5 cm/min

Thickness = 4 mils

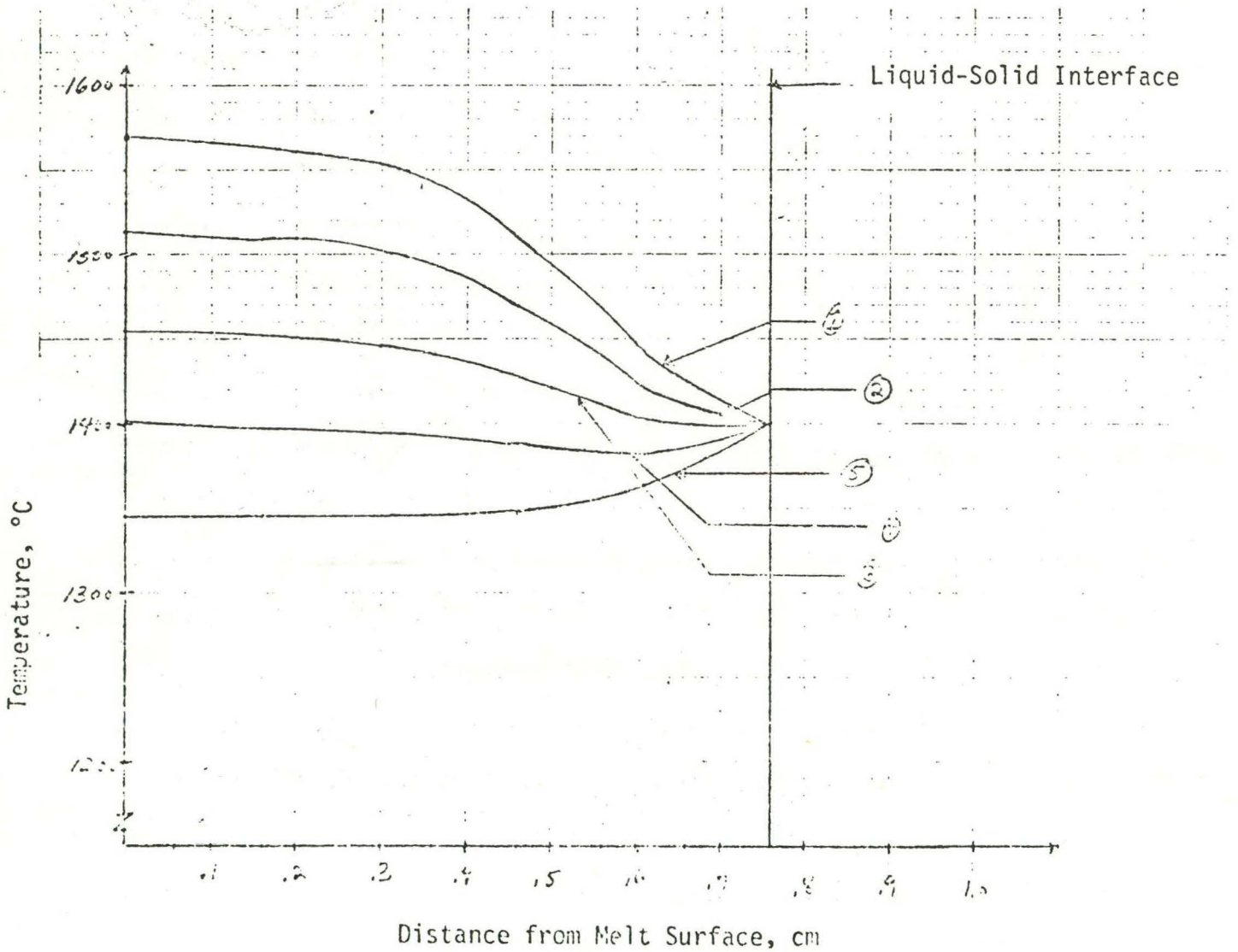

Figure 24. Temperature of the melt in the meniscus as a function of distance above the melt surface. Liquid surface interface is located at 0.76 cm.

Graph of Temperature of Melt Surface
vs.
Pull Rate of Web Growth

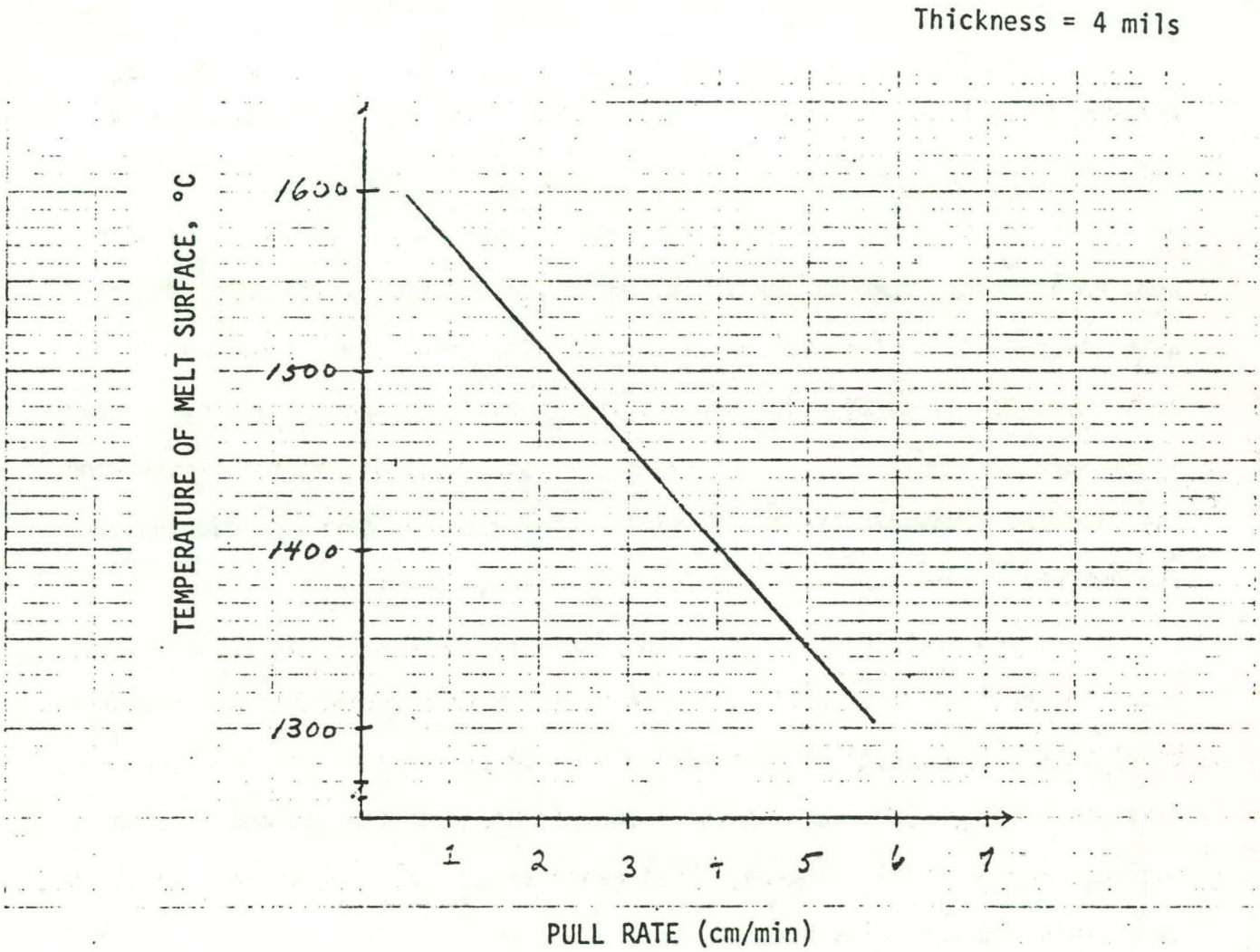

Figure 25. Temperature of melt surface as a function of pull rate.

The primary conclusion that can be drawn is that there may be a single pull rate applicable to a given furnace thermal geometry. Although there may be some tolerance on the value, accurate control of pull rate may be required.

Thermal Model of the Melt, Crucible, Susceptor, and Lid.

Figure 26 shows the nodal geometry for the thermal model presently being used to represent heat transfer in the melt, crucible, susceptor, and lid.

As a result of the thermal effect of the slot in the lid and the web, an azimuthal temperature variation in temperature exists which causes a three-dimensional temperature variation. The three dimensional nodal geometry is obtained by sectioning at increments of azimuthal angle. However, it is seen in Figure 27 that the symetry exists about diametrical lines along the slot and perpendicular to the slot. Consequently, thermal modeling of the 90° section is sufficient to determine the temperature field.

Induction heating by the RF field is present primarily in the outer periphery of the susceptor. The nodes in this region have a thickness equal to the skin depth of approximately 0.059 cm and are seen in Figure 26. Heat generation also occurs in the outer periphery of the lid and is also included in the model. Internal heat generation is assumed uniform up to the skin depth and zero elsewhere.

The lid is heated by radiation heat transfer from the silicon melt and the crucible. The lid in turn radiates heat to the surroundings from the upper surface. Conduction and convection heat transfer to the argon atmosphere also effects the lid temperature.

The LION-4 computer program is being used to calculate the temperature field. The internal heat generation rate is specified and from that the

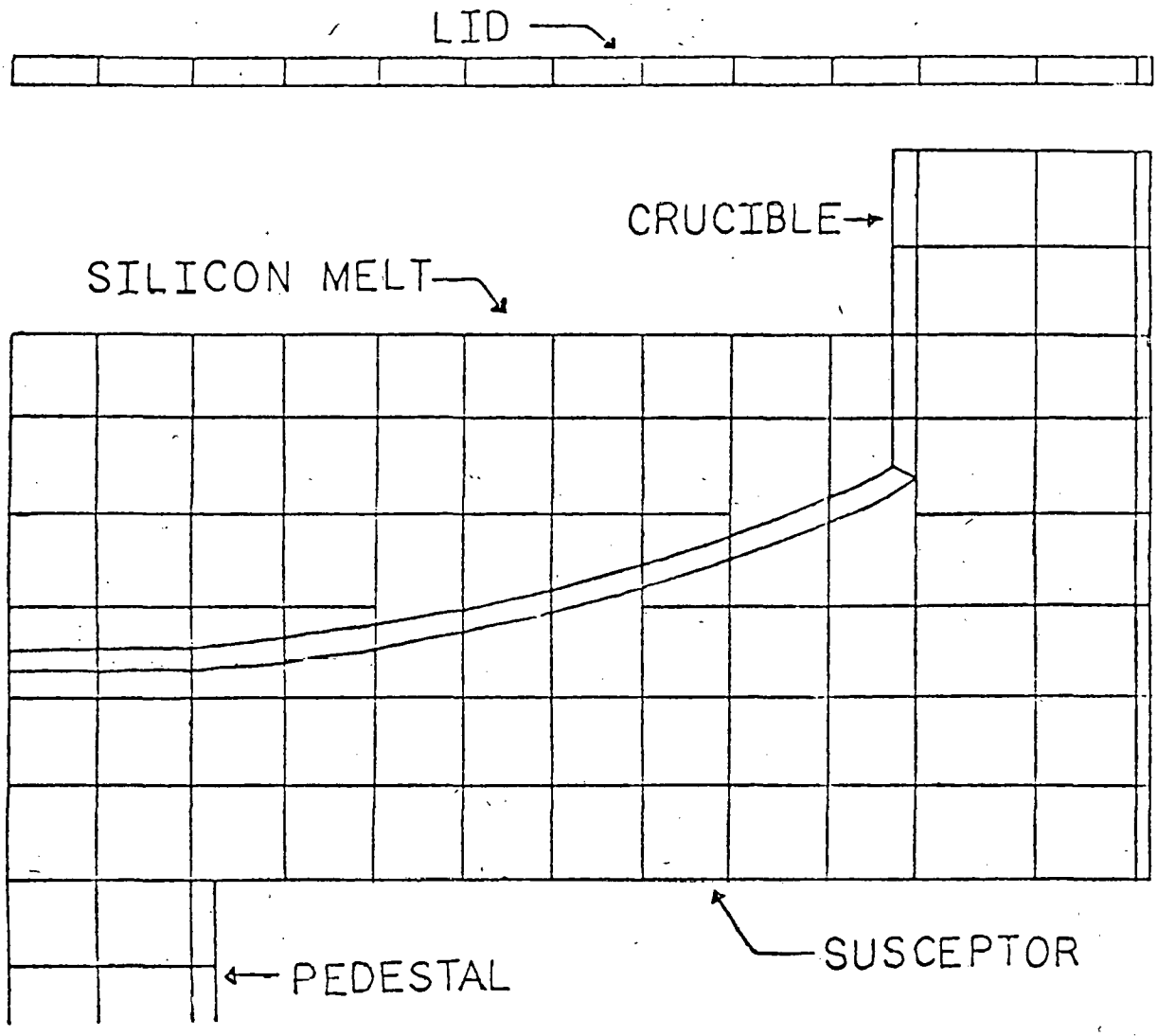

Figure 26 Thermal Model Modal Geometry Melt Crucible, Susceptor, and Lid

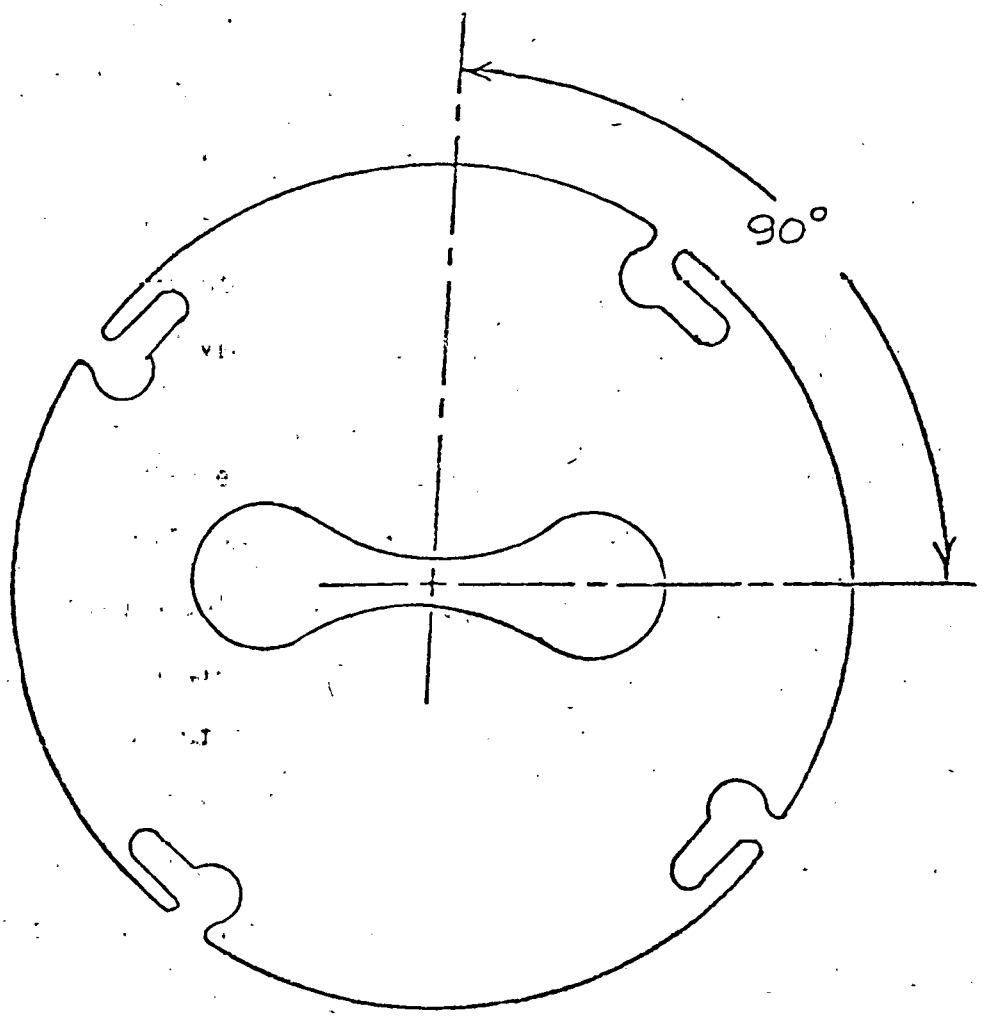

Figure 27. Temperature Field of Each 90° Sector is Identical Due to Symmetry.

temperatures are calculated.

The temperature distribution in the melt, crucible, and susceptor were determined using the two-dimensional model and the results are shown in Figure 28. The calculation was performed for a solid lid and the effect of the web was not included in the calculations. The temperature distribution in the silicon melt is of primary importance since it is a determining factor in obtaining web growth. Investigations are presently underway to evaluate the calculated temperatures to determine whether they are ideal for web-growth. It seems that the decreasing temperature gradient from the melt surface to the bottom of approximately 4 °C may be encouraging to excessive dendritic growth.

Temperature probe data taken at the bottom of the melt appear to agree with the calculated values. However, the calculated lid temperatures are approximately 200 °C below measurements. Two explanations for the inaccuracy are currently under investigations. First, the emissivities of the silicon melt and molybdenum are subject to inaccuracies. It was assumed in the calculations that the emissivity of silicon melt and molybdenum are 0.2 and 0.37, respectively. A higher emissivity of silicon melt, for example, would result in increased thermal coupling between the silicon melt and lid causing the lid temperature to increase.

Secondly, the induction heating assumed for the lid may be significantly larger than assumed. It was assumed in the results contained in Figure 28 that induction heating would occur in the outer periphery at a radial distance equal to the skin depth. The assumed region of internal heat generation in the lid is the small node at the edge of the lid in Figure 28. The induction field may be sufficiently large at the top of the lid to cause additional heating. In Figure 29, the induction field lines obtained by electric field analogy

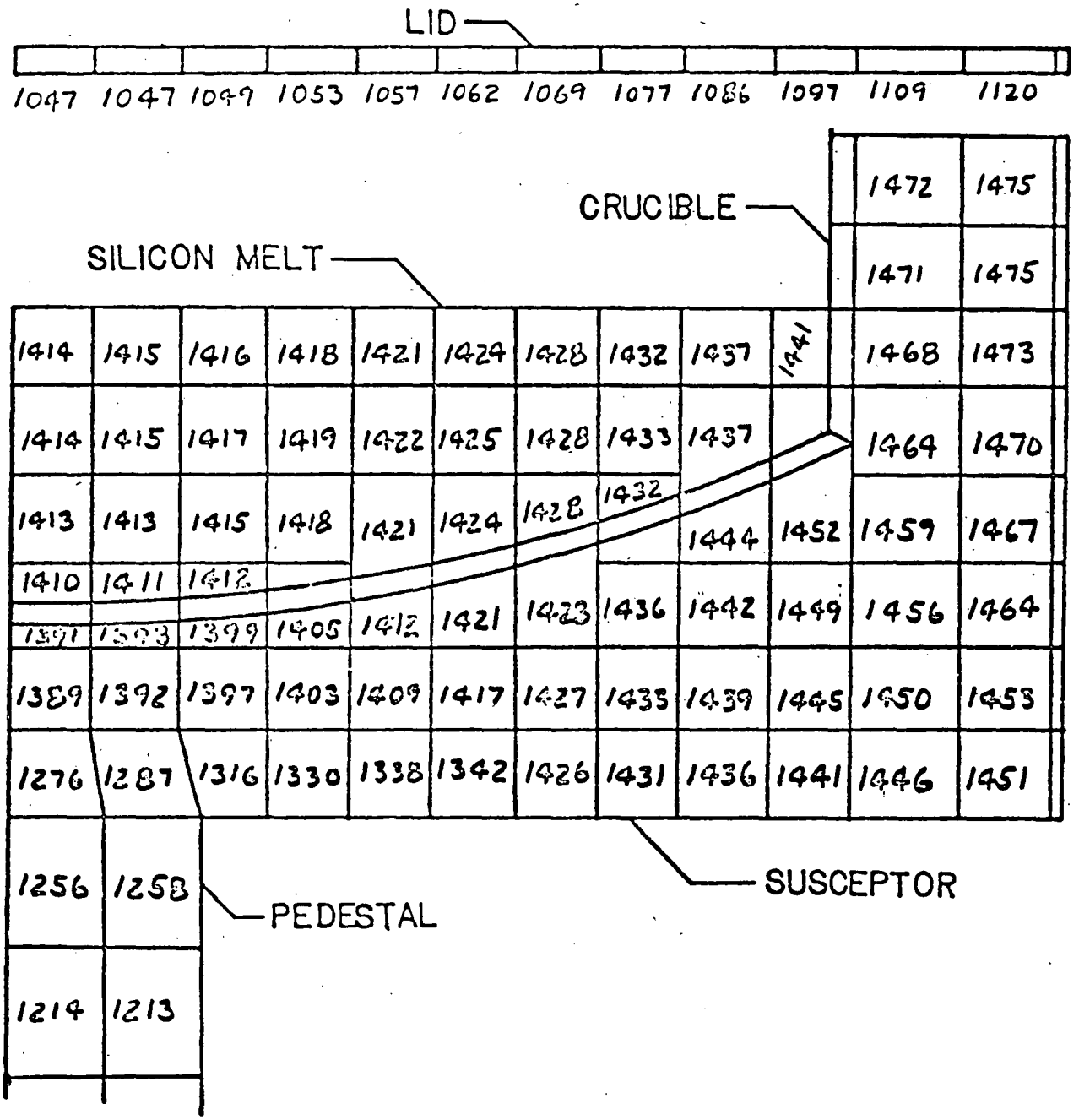

Figure 28. Calculated Temperature Distribution in the Melt, Crucible, and Susceptor. Temperatures in °C.

INDUCTION FURNACE MAGNETIC FIELD

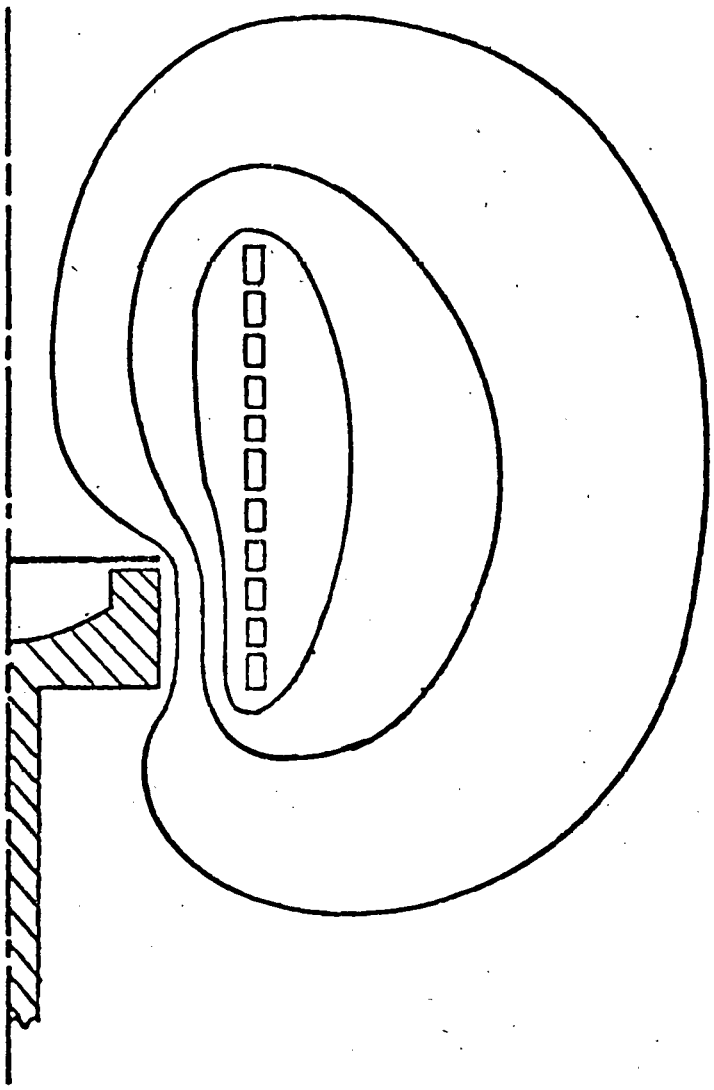

Figure 29. Furnace Induction Field Geometry, Determined by Electric Field Analogy.

are shown and it is seen that the lines curve rather sharply over the top of the lid which could result in significant induction heating.

Bibliography

1. Swartz, J.C., T. Surek, and B. Chalmers, "The EFG Process Applied to the Growth of Silicon Ribbons", J. of Electronic Materials, Vol. 4, No. 2, 1975, pp. 255-279.

2. Batchelor, G.K., An Introduction to Fluid Dynamics, Cambridge at the University Press, 1967, pp. 63-68.

3. Gaule, G.K.and J.R. Pastore, "The Role of Surface Tension in Pulling Single Crystals of Controlled Dimensions", Metallurgy of Elemental and Compound Semiconductors, Ed. by R. O. Grubel, Interscience Publishers, N.Y., 1961, pp. 201-226.

4. Mika, A. and W. Uelhoff, "Shape and Stability of Menisci in Czochralski Growth and Comparison with Analytical Approximations", Journal of Crystal Growth, Vol. 30, 1975, pp. 9-20.

5. O'Hara, S. and A.I. Bennett, "Web Growth in Semiconductors", Journal of Applied Physics, Vol. 35, No. 3, 1964, pp. 686-693.

Web Characterization

During this report period the facilities for characterizing the seed dendrites and dendritic-web samples have been set up and made operational. This topic is divided into two general areas, structural and electrical, the activity in each of which is summarized below.

Structural.

Measurement of twin spacings, thickness, density of dislocations running down the web parallel to the two main faces, and spacing of twin lamellae between the main faces necessitate viewing the sample "end on" under an optical microscope. This requires very exacting alignment. Often it is desired to tilt the sample approximately 20° to examine one of the {111} planes on the fracture cross-section. The sample holder itself shown in Figure 30 was fabricated from a 1/4 inch diameter steel rod with one end machined flat and a wire spring attached so that the sample is held firmly against the flat. The rod is placed in a V cut in a small block of steel that is affixed on one side of a steel plate cut to the size of a microscope slide. A knob allows rotation of the sample.

Transmission electron microscopy is used to examine samples for dislocations and microdefects (vacancy cluster, dislocation loops, and microprecipitates). One-eight (1/8) inch diameter samples must be cut to fit on the standard electron microscope sample grids. The samples must then be thinned to less than 2000 Å. A tool was made for the ultrasonic cutter to cut 1/8 inch diameter samples. Tests are being made to be sure that the cutter we use is not putting in damaged or additional dislocations.

Thinning of such small samples for TEM requires jet etching. Jet etchers for Si and Ge require special materials that can withstand

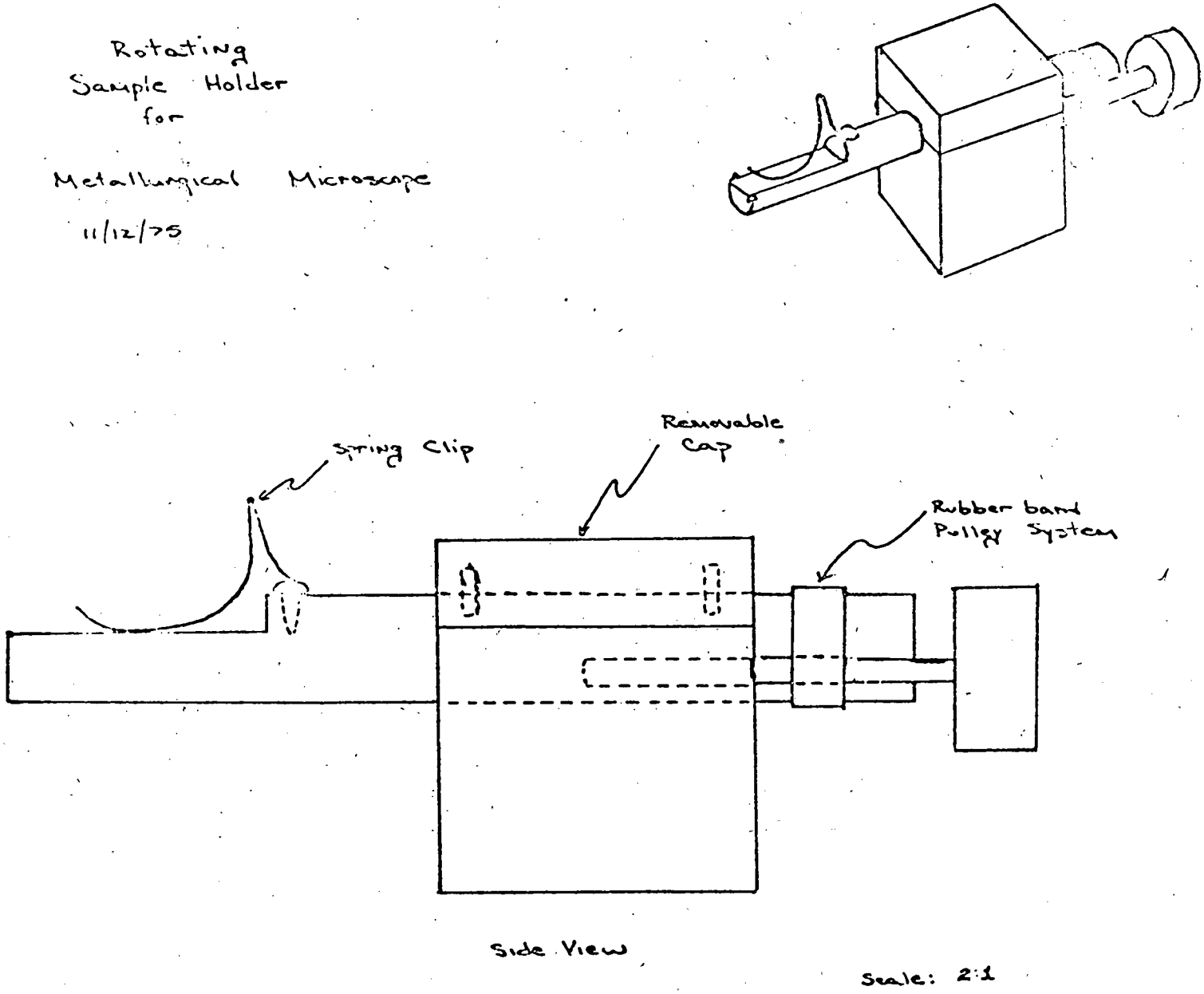

Figure 30. Rotating Sample Holder

HNO_3 and HF and also not introduce contamination. A jet etching apparatus has been designed and constructed somewhat along the lines of several already reported in the literature. The first design proved to be too critical in adjustment and gave very uneven etching. A second one has been built.

With the new instrument and practice an operator can repeatedly produce successfully etched samples. The active nature of the etchant is a constant worry, but immediate clean-up of the etcher after use minimizes part wear. Parts that wear are the tip and the bottom cap of the nozzle which are made of quartz.

The following is a description of the modifications made on the etcher, and a detailed etching operation procedure is given in Table 2.

As depicted in Figure 31, the nozzle body is made of teflon instead of quartz as used before. Since the CP4 etchant does not react with teflon, the problem of erosion is eliminated. The tip is made of a piece of quartz capillary with an inside diameter 1 mm. It is sealed to a holder which screws into the nozzle body. The holder is also made of teflon. The etchant does erode the tip and the bottom cap. If care is taken in thoroughly cleaning the nozzle after each etching operation, the tip and the bottom cap can last for many operations.

In order to evaluate the role of twin spacing in the seed dendrites on the growth of dendritic-web ribbon a number of primitive dendrites were grown containing the number of twin planes and twin plane spacings given in Table 3.

The number of twins and the twin plane spacings of the dendritic-web samples grown from seeds of known twin plane characters are given in Table 4.

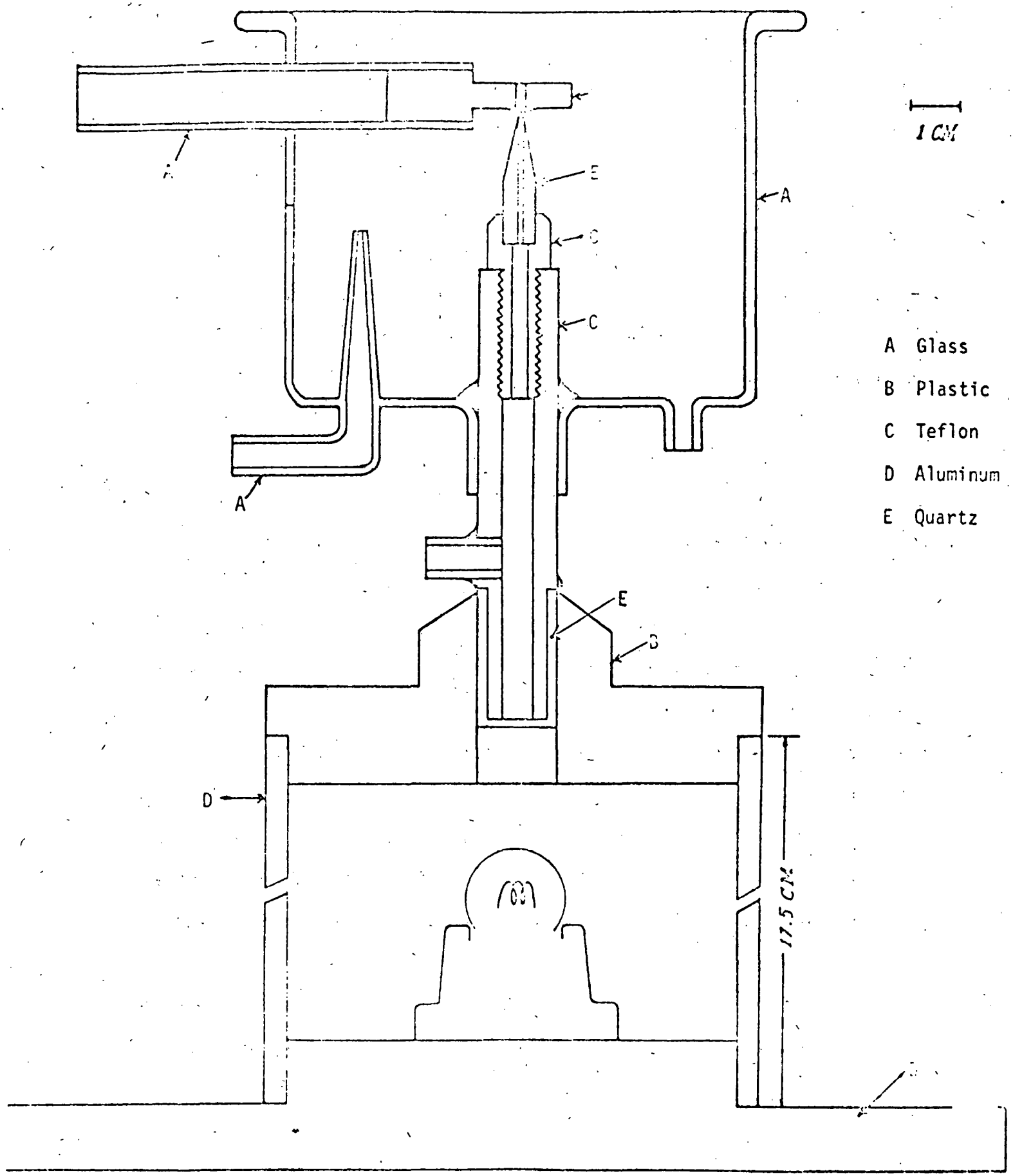

Figure 31. Jet Etching Apparatus

TABLE 2

OPERATION PROCEDURES FOR THE JET ETCHER

PRECAUTION: Protective gloves should be worn during entire operating procedure

1. Insure that drain reservoir is properly connected to etcher drain and charged with the necessary $CaCO_3$ + $CaCl_2$ + H_2O acid neutralizer.
2. Mount the sample to the holder with black wax. (Use toluene as solvent.)
3. Position the sample above the nozzle tip. The distance between the sample and the tip should be approximately 3 mm.
4. Place the top on the etcher. Assure that the sample can be observed from the viewing mirror.
5. Adjust the bottom of the etchant reservoir to a level approximately 5 cm above the nozzle tip.
6. Mix CP4 etchant. (To etch a 10 mil silicon sample, use 27 c.c. HF + 123 c.c. HNO_3.)
7. Turn on rinse jet water.
8. Turn on the etcher light.
9. Turn off the room light.
10. Pour etchant into the reservoir.
11. When a dim red light is observed in the viewing mirror, reposition the sample holder so that the sample is directly above the rinse jet.
12. Turn on the room light.
13. Decant the residual etchant from the reservoir into a plastic beaker.
14. Disconnect the tubing from the reservoir to release the remaining etchant into the beaker.
15. Stop the rinse jet water.

16. Remove the sample holder and rinse it in water.
17. Disconnect tubing from the rinse jet.
18. Remove tubing form the drain reservoir.
19. Rinse the etcher with tap water.
20. Unscrew the nozzle tip holder from the nozzle body and rinse both parts thoroughly with water.
21. Remove the sample from the holder. (Dissolve wax in toluene.)
22. Rinse the sample in acetone.

TABLE 3

Table of Twin Spacings from Primitive Dendrite Pulls

No. of Twin Planes	Twin Plane Spacings (μm)			
	1	2	3	4
5	0.4	0.4	0.1	1.9
4	1.6	2.4	1.0	
	8.0	2.0	10.0	
	19.2	1.0	8.8	
3	2.0	1.0		
	4.0	1.0		
	4.4	2.0		
	8.0	2.0		
	1.9	0.8		
	8.8	1.0		
	0.8	0.6		
	8.5	0.3		
2	14.0			
	12.0			
	9.4			
	7.0			
	6.4			

TABLE 4

Twin Spacings in Dendritic-web Samples

SAMPLE:	7-6-76-C-3	
	SEED:	5 Twins Spacings: 1.6μ, .45μ, .10μ, .45μ.
	3 Regions	a) 5 Twins 2μ, 2μ (4 Twins) b) 3 Twins 27μ, 0.15μ. c) 4 Twins 27μ, 2.4μ (3 Twins)
SAMPLE:	7-6-76-C-2	
	SEED:	5 Twins Spacings 1.6μ, .45μ, .10μ, .45μ.
	5 Regions	a) Web, no Twin b) 1 Twin c) 2 Twins 26μ d) 6 Twins 26μ, 1.8μ, 0.1μ, 0.1μ, 1.8μ. e) 2 Twins 26μ.
SAMPLE:	6-28-76-D-4	
	SEED:	5 Twins 1.6μ, .45μ, .10μ, .45μ
	5 Twins	Run through the entire sample, same spacing as seed.
SAMPLE:	6-25-76-F-2	
	SEED:	5 Twins 1.6μ, .45μ, .10μ, .45μ. Sample has only 3 Twins 1.7μand 0.2μ.
SAMPLE:	6-28-76-D-2 #2	
	SEED:	5 Twins 1.6μ, .45μ, .10μ, .45μ.
	2 Regions	5 Twins in both regions Spacings 1.6μ, .45μ, .10μ, .45μ. The twins from two regions do not meet.
SAMPLE:	6-28-76-D-1	
		Twin structure is the same as 6-28-D-2 #2.
SAMPLE:	6-28-76-D-2 #1	
	SEED:	5 Twins 1.6μ, .45μ, .10μ, .45μ.
		Twin in web is the same as in seed.

Table 4 (continued)

SAMPLE:	7-7-76-C	
	SEED	3 Twins 8μ, 2μ. 3 Twins run across the entire sample. Spacing measures 8μ, 1.75μ.
SAMPLE:	6-17-76-A	5.6
	SEED	5 Twins 2μ, 1μ(4 Twins)
	5 Regions	a) 5 Twins: 2μ, .8μ, (4 Twins) b) 3 Twins: 1.2μ, .8μ. c) 3 Twins: .25μ, 1.75μ. d) 7 Twins: .25μ, 1.75μ, 2μ, .9μ(4 Twins) e) 5 Twins: 2μ, .9μ(4 Twins)
SAMPLE:	6-17-76-C-4	
	SEED	5 Twins 2μ, 1μ(4 Twins)
	4 Regions	a) 5 Twins 2μ, 1μ(4 Twins) b) 3 Twins c) 1 Twin } Too small for optical measurement d) 4 Twins

Electrical

Facilities for making the following electrical characterization measurements have been completed and tested:

1. Van der Pauw
2. Four point probe resistivity
3. Hot probe conductivity type monitor
4. MOS minority carrier lifetime
5. Solar cell dark and illuminated i-v characteristics.

Work has been carried out to develop a technique for applying contact test patterns on narrow web (less than 5 mm) in order to electrically characterize these materials. Conventional techniques used for wafers have been found inappropriate due to geometric difficulties with the small size samples and irregular surfaces.

The development of a prototype projection masking system was completed for this purpose. Using this system a series of MOS structures for lifetime measurements have been fabricated on dendritic-web samples, approximately .75 cms. wide, without removal of the edge dendrites. These patterns have also been applied to non-planar samples directly on top of a dendrite such that the pattern covered part of the dendrite and part of the web. The system consists of a photographic enlarger used to project the mask image which is illuminated by a UV light source.

Data was collected during this report period on the resistivity and charge carrier type of several dendritic-web samples. In all cases the samples were p-type ranging in resistivity from 2 to over 100 ohm-cms. Representative data of these measurements is given in Table 5.

A model has been developed and tested on Czochralski wafers for analysis of the data from MOS transient capacitance measurements to obtain both the surface recombination/generation lifetime and the minority carrier

TABLE 5

Data on Resistivity

Sample	Type	Resistivity (ohm-cm)
2-23-76-A-2	P	2.33
3-19-76-A-2	P	3.55
4-7-76-E-5	P	5.10
4-7-76-F-16	P	6.06
3-19-76-A-1	P	7.65
3-8-76-A-1	P	8.13
3-8-76-A-3	P	10.03
4-7-76-E-1	P	11.48
4-7-76-F-1	P	12.70
2-23-76-A-1	P	13.86
3-19-76-A-9	P	15.70
3-19-76-A-10	P	16.50
4-7-76-A-2	P	18.40
2-23-76-B-2	P	19.70
4-2-76-B-1	P	20.90
4-2-76-A-1	P	22.18
4-7-76-E-3.5	P	34.34

generation lifetime. This model is based on a compromise between the one proposed by Heiman (6) and that proposed by Zerbst (7). Heiman chose in his analysis to ignore the effect of the surface recombination by using only the data from the latter part of the MOS transient response. Zerbst on the other hand included the effect of the surface recombination, but considered it to be a time invariant parameter during the entire duration of the transient MOS response. The model proposed here treats the surface recombination/generation effects as constants only during the very initial (0.2%) portion of the transient response, where its effect on the results is greatest; and then allows it to drop off to zero at the end of the response, as it should. The time dependance of this drop-off results from the analysis of the MOS transient response.

From Heiman's work, the rate of change of the surface density of electrons in the inversion layer of a p-type sample is given by:

$$\frac{dN_s}{dt} = \frac{n_i}{2\tau} \quad (W - W_f) \ , \tag{8}$$

where: N_s = surface density of electrons
n_i = intrinsic charge carrier concentration
τ = minority carrier generation lifetime
W = depletion layer width
W_f = depletion layer width at end of transient response.

(6) Heiman, I.E.E.E. Trans Elec Devices, ED-14, 11, 781-4(1967)

(7) Zerbst, F. Angew, Phys, 22, 30-3 (1966)

In terms of capacitance, normalized to the oxide capacitance, equation (8) can be rewritten as:

$$\frac{dN_s}{dt} = \frac{n_i}{2\tau}\left(\frac{\varepsilon_s}{\varepsilon_{ox}}\right)T_{ox}\left(\frac{1}{C} - \frac{1}{C_f}\right), \tag{9}$$

where: ε_s = permittivity of the semiconductor
ε_{ox} = permittivity of the oxide
T_{ox} = thickness of the oxide
C = normalized MOS capacitance
C_f = normalized MOS capacitance at end of transient.

Now if the effects of surface recombination/generation are to be included, as is done by Zerbst, a term to account for this must be added to (9), i.e.:

$$\frac{dN_s}{dt} = \frac{n_i}{2\tau}\left(\frac{\varepsilon_s}{\varepsilon_{ox}}\right)T_{ox}\left(\frac{1}{C} - \frac{1}{C_f}\right) + \left(n_i/2\right)S, \tag{10}$$

where: S = surface recombination/generation velocity.

Heiman states that the time, T, required to generate enough carriers to neutralize the entire depletion region is given by:

$$T = 2\tau\,\frac{N_a}{n_i}, \tag{11}$$

where: N_a = doping density.

Using equation (8), (11) can be rewritten as:

$$\frac{dN_s}{dt} = \frac{N_a}{T} (W - W_f). \tag{12}$$

Heiman also gives the following expression for the time rate of change of the normalized capacitance:

$$\frac{dC}{dt} = \frac{C^2}{T}\left(1 - \frac{C}{C_f}\right). \tag{13}$$

Substitution for T from (13) in (12) gives, when the depletion widths are expressed in terms of capacitors:

$$\frac{dN_s}{dt} = \frac{dC}{dt} \frac{T_{ox} N_a}{C^3}\left(\frac{\varepsilon_s}{\varepsilon_{ox}}\right). \tag{14}$$

Equations (10) and (14) can be equated to give

$$\frac{dC}{dt} \frac{T_{ox}N_a}{C^3}\left(\frac{\varepsilon_s}{\varepsilon_{ox}}\right) = \frac{n_i}{2\tau}\left(\frac{\varepsilon_s}{\varepsilon_{ox}}\right) T_{ox}\left(\frac{1}{C} - \frac{1}{C_f}\right) + \left(\frac{n_i}{2}\right) S. \tag{15}$$

Equation (15) involves two unknowns, τ and S. If it is assumed that S is constant during the initial part of the transient response, equation (15) can be evaluated at two of the initial points of the transient response giving two equations in two unknowns which can be solved directly. Using the value of τ found from this procedure the value of S can be computed

from (15) for the remainder of the transient response.

This model and procedure was tested on a Czochralski grown p-type wafer with the results giving good agreement with what was expected for τ, i.e. $\tau = 0.3$ μ secs. The value for S was of the order given by Zerbst for typical samples using the MOS transient response but was negative in value indicating that the surface states present were acting as recombination rather than generation centers. The values of S so obtained are plotted in Figure 32.

In order to evaluate the web-dendritic silicon for solar cells, it was decided that as a minimum the i-v characteristics and efficiencies of representative cells must be measured.

An Eppley pyrometer has been set up to measure the sun's insolation during the solar cell testing, which is done by natural sunlight.

A test circuit has been completed for making both the dark and illuminated i-v characteristics of solar cells with a dynamic display of the results under loading conditions ranging from zero to infinity. The circuit is shown in block form in Figure 33, and schematically in Figure 34. Two controls are available to the operator for setting the current amplitude and the offset bias. The output which is displayed on an oscilloscope is the i-v characteristic of the test solar cell.

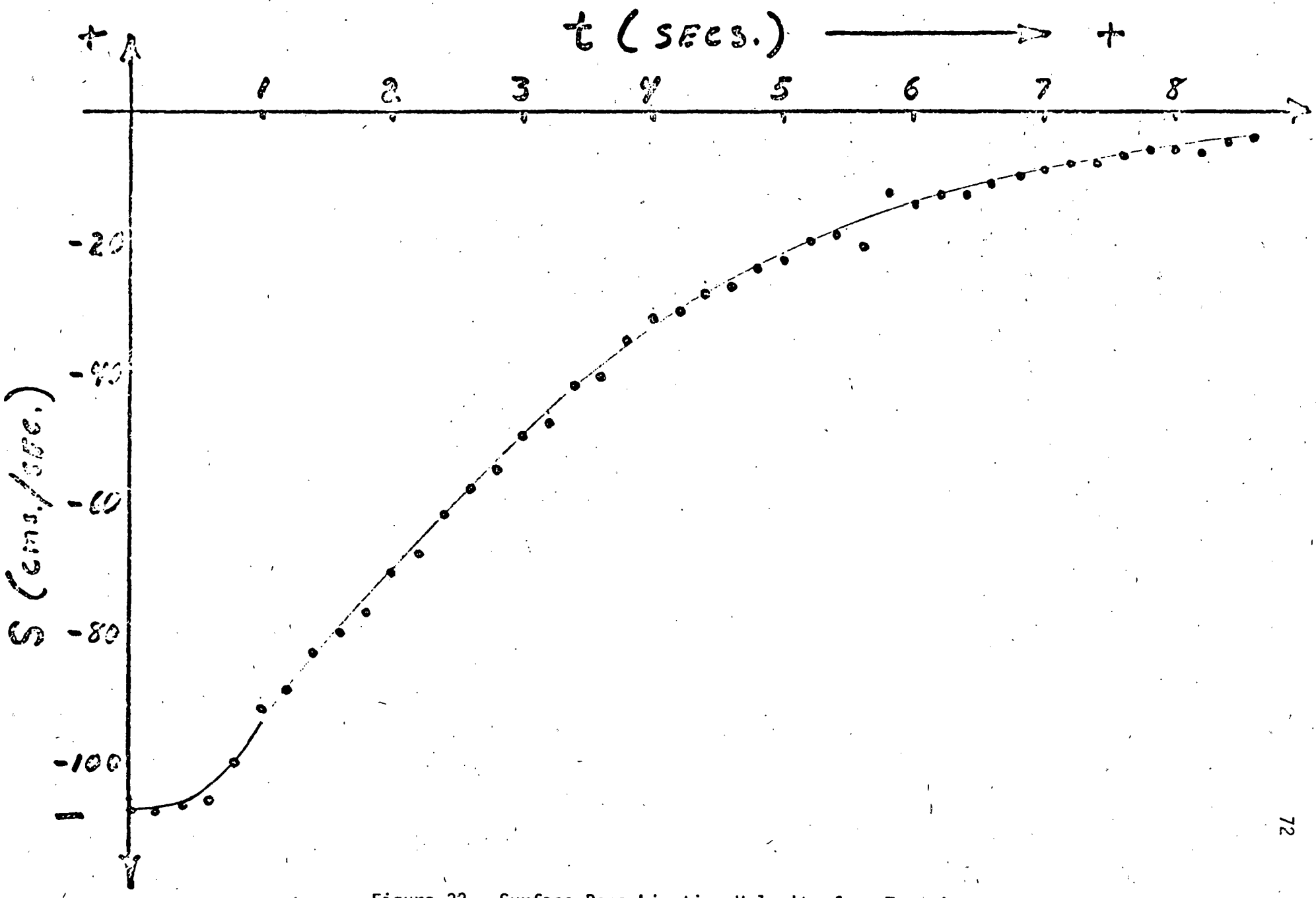

Figure 32. Surface Recombination Velocity from Transient MOS Capacitance

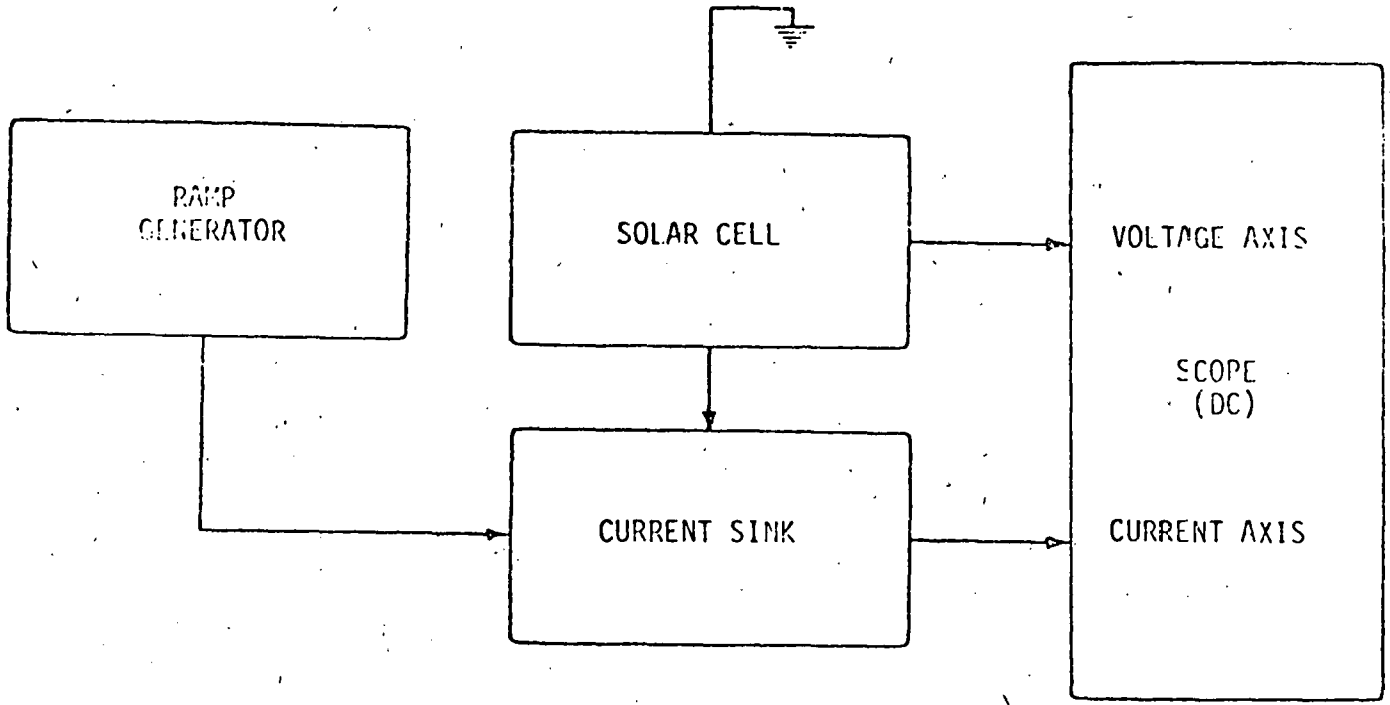

Figure 33. BLOCK DIAGRAM OF TESTER

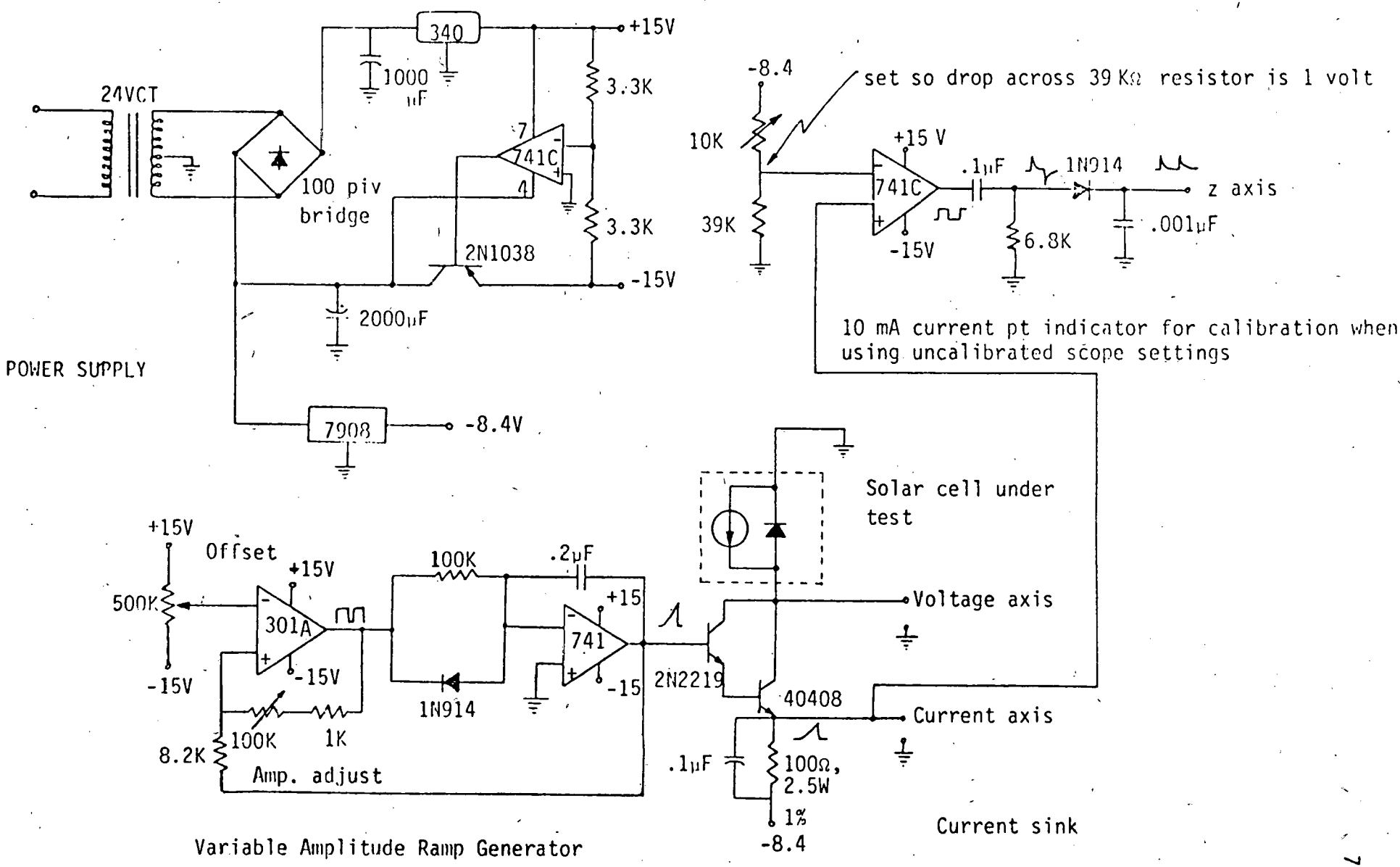

Figure 34. Solar Cell I - V Tester
Capable of sweeping currents from 1 to 200 mA.

Engineering Drawings

The majority of the drawings and sketches are given in the text of this report as Figures 1 - 34.

The figures given in this section represent additional drawings and sketches that were generated during this report period.

Figure 35 is a schematic of the circuit used to interface between the temperature controller used on the growth furnace and the generator that furnishes power to the furnace.

Figure 36 is a plot giving the speed of the take-up reel on the growth furnace as a function of the control variac setting. The reel speed is the same as the pull rate of the dendritic-web being wound up on it.

Figure 37 is a sketch of the seed holder which holds the dendrite seed to the stainless steel ribbon attached to the take-up reel of the growth furnace.

Figure 38 is a sketch of the apparatus put together for making the transient MOS capacitance measurements for the determination of minority carrier lifetime.

CONTROLLER TO GENERATOR INTERFACE CIRCUIT

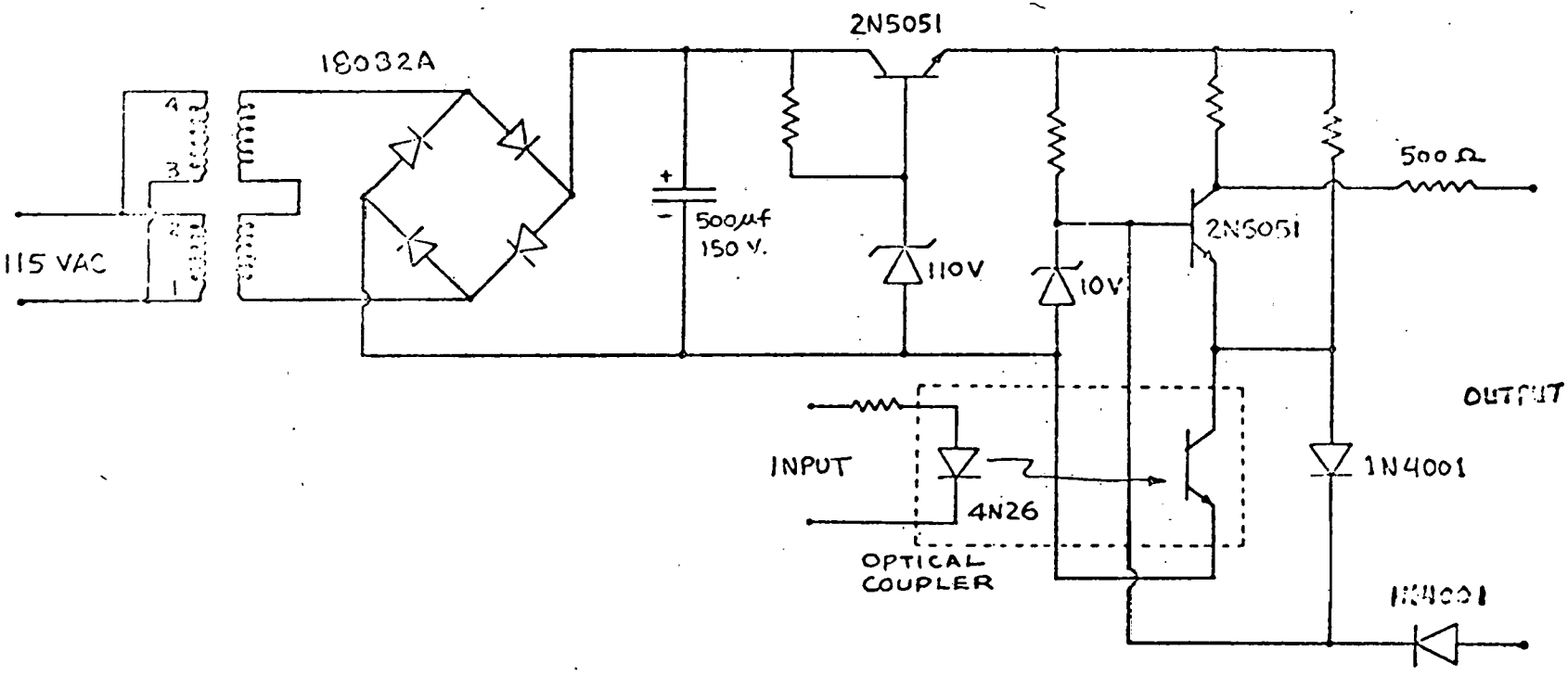

Figure 35

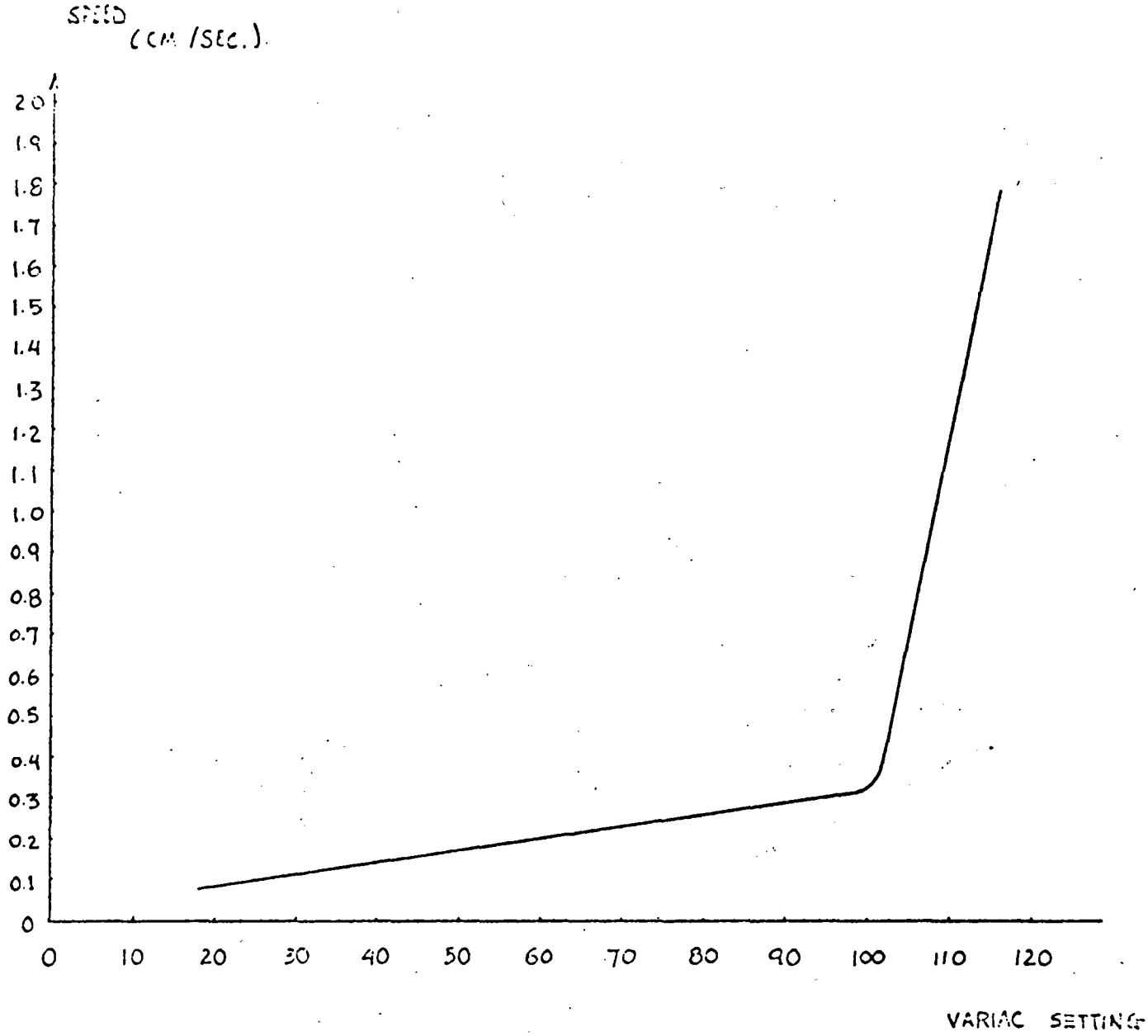

REEL SPEED AS A FUNCTION OF VARIAC SETTING (115 VOLT LINE)

Figure 36

SEED HOLDER

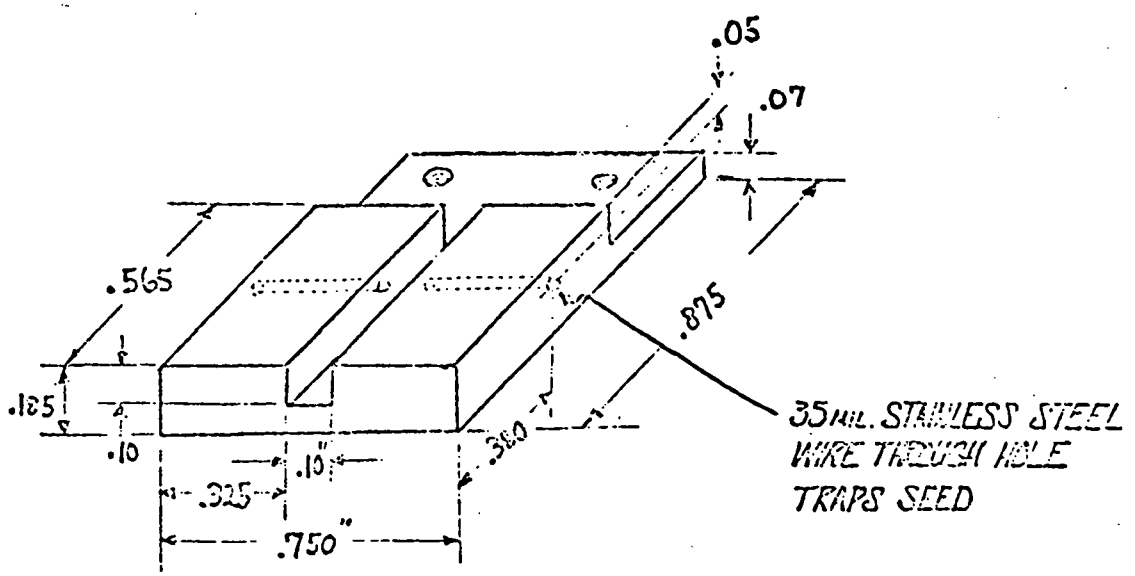

Figure 37

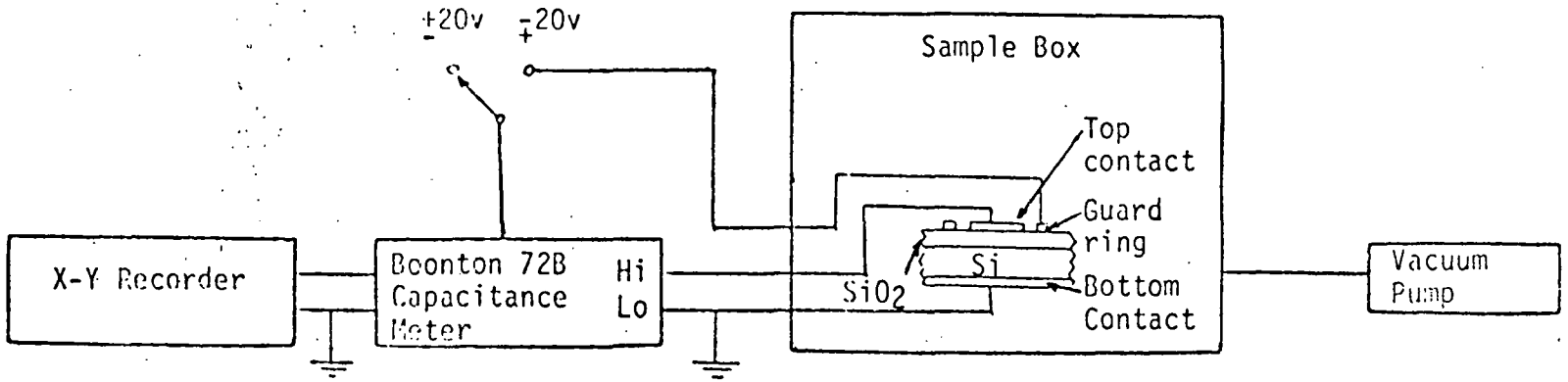

Figure 38 MOS Capacitance Lifetime Measuring Apparatus

Sample Box: Approximately $(2 \text{ feet})^3$ constructed of 3/4 inch plywood lined with 1/32 inch aluminum so as to be light and electrically tight. The box is cut on a side diagonal and hinged on the upper rear edge so as to open in a clam-shell fashion. It contains a binocular microscope, a probe positioner ring, and two vacuum sample stages.

Projection of Next 6 Month's Activities.

During the next few months, the major effort of this contract will be in establishing the thermal profile in the furnaces and the proper techniques for growing two dendrite web in a reproducible fashion. Once this has been accomplished extensive thermal probing data will be collected to document the criteria required for two dendrite web growth. Experiments will then be performed to determine the range of thermal conditions over which it is possible to grow two dendrite web. Using this data in our computer models of the growth facility, the maximum limits on growth width and pull rate for two-dendrite web will be ascertained by thermal analysis. In addition, the results of the thermal analysis studies will be used to determine what changes in the growth furnace and pulling procedures will be necessitated in order to increase the width and pull rate of two-dendrite web.

In conjunction with the above activity all web samples will be characterized both structurally and electrically in order to maintain the quality necessary for photovoltaic solar cells.

Summary of Characterization Data.

The characterization data generated during this report period is found throughout the text of this report as follows:

PROGRAM PLAN

WEB-DENDRITIC RIBBON GROWTH

UNIVERSITY OF SOUTH CAROLINA

PERIOD: 1 OCTOBER 1975 - 1 MAY 1977

UPDATED 31 SEPTEMBER 1976

CONTRACT NO. 954344

LECEND:
H - HILBORN
F - FAUST
R - RHODES
A - RESEARCH ASSOCIATE
G - GRADUATE ASSISTANT
S - SECRETARY

(Figures in columns represent man hours committed)

1. Web Growth, Growth Analysis

1.1 Set up web furnace

1.1.1 Level, align, calibrate gas flow, measure physical/mechanical parameters

1.1.2 Instrument melt temperature sensors, run furnace and RF generator

1.1.3 Calibrate RF generator controls to melt temperature, no web pulling

1.2 Web growth, manual batch

1.2.1 Pull nominal web based on 1965 experience, establish measurements baseline. (Instrument melt level measurement), correlate with crystallization kinetics and seeding requirements

1.2.2 Vary pull rate, measure effects, correlate with crystallization kinetics and seeding requirements

1.2.3 Vary RF heat transfer rate, measure effects, correlate with crystallization kinetics and seeding requirements

1.2.4 Couple RF heat transfer rate and pull rate variations, measure effects, correlate with crystallization kinetics and seeding requirements

1.2.5 Final experimental design

1.2.6 Final manual variation of manipulated variables, correlation with crystallization kinetics and seeding requirements

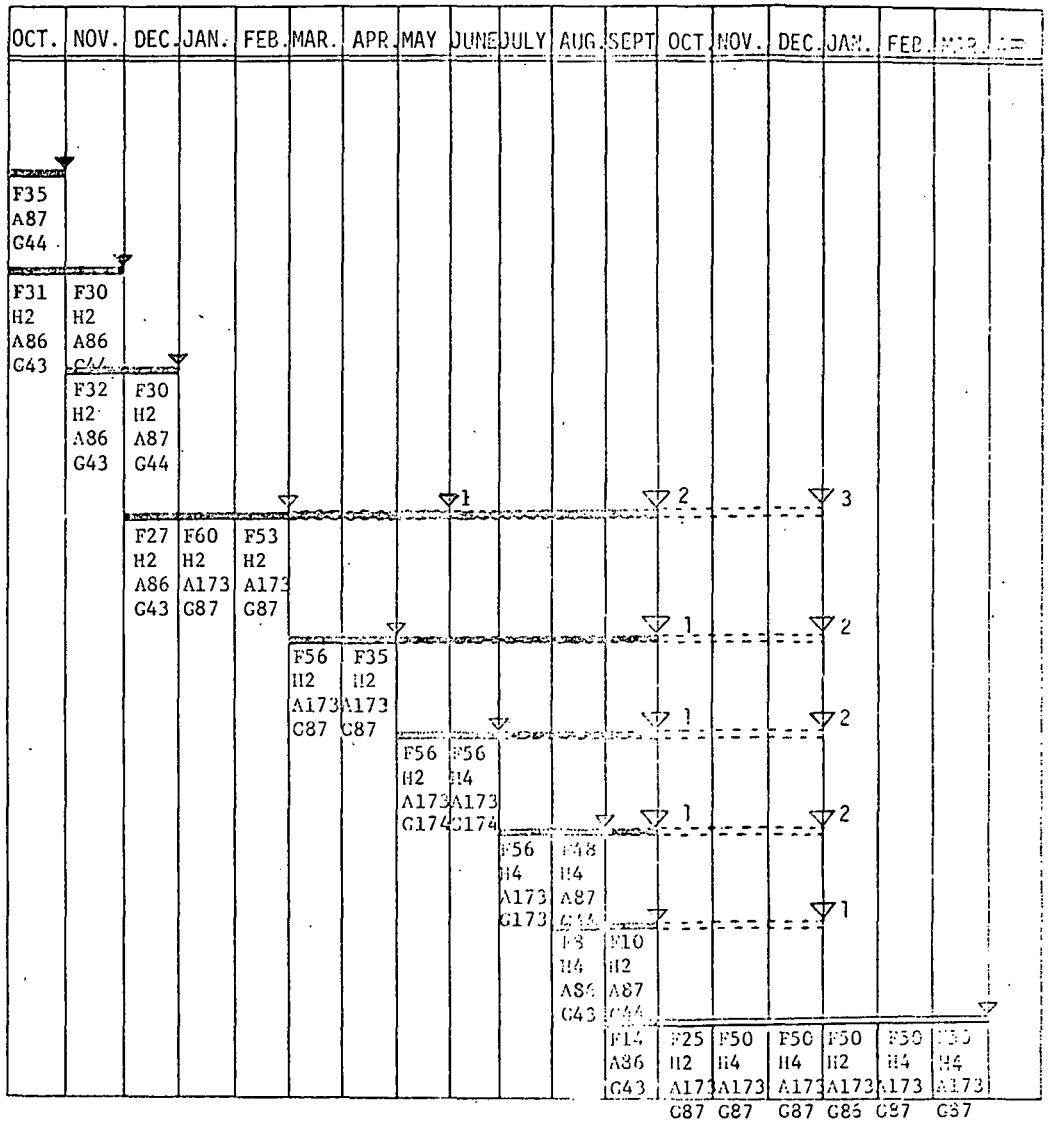

1.3 Web growth analysis

1.3.1 Develop semi-empirical multivariate static model from web growth manual experiments

1.3.2 Thermal web growth analysis

1.3.3 Correlate analysis, experimental data, and semi-empirical model

2. Web Characterization

2.1 Development of sampling strategy, prototype technique

2.2 Structural characterization

2.3 Electrical characterization, web bulk silicon

2.4 Electrical characterization, web solar cells

3. Documentation, Program Review

3.1 Documentation

3.1.1 Initial financial management report and program plan

3.1.2 NASA Form 533M MAR 73, JPL 3645, JPL 3645-1

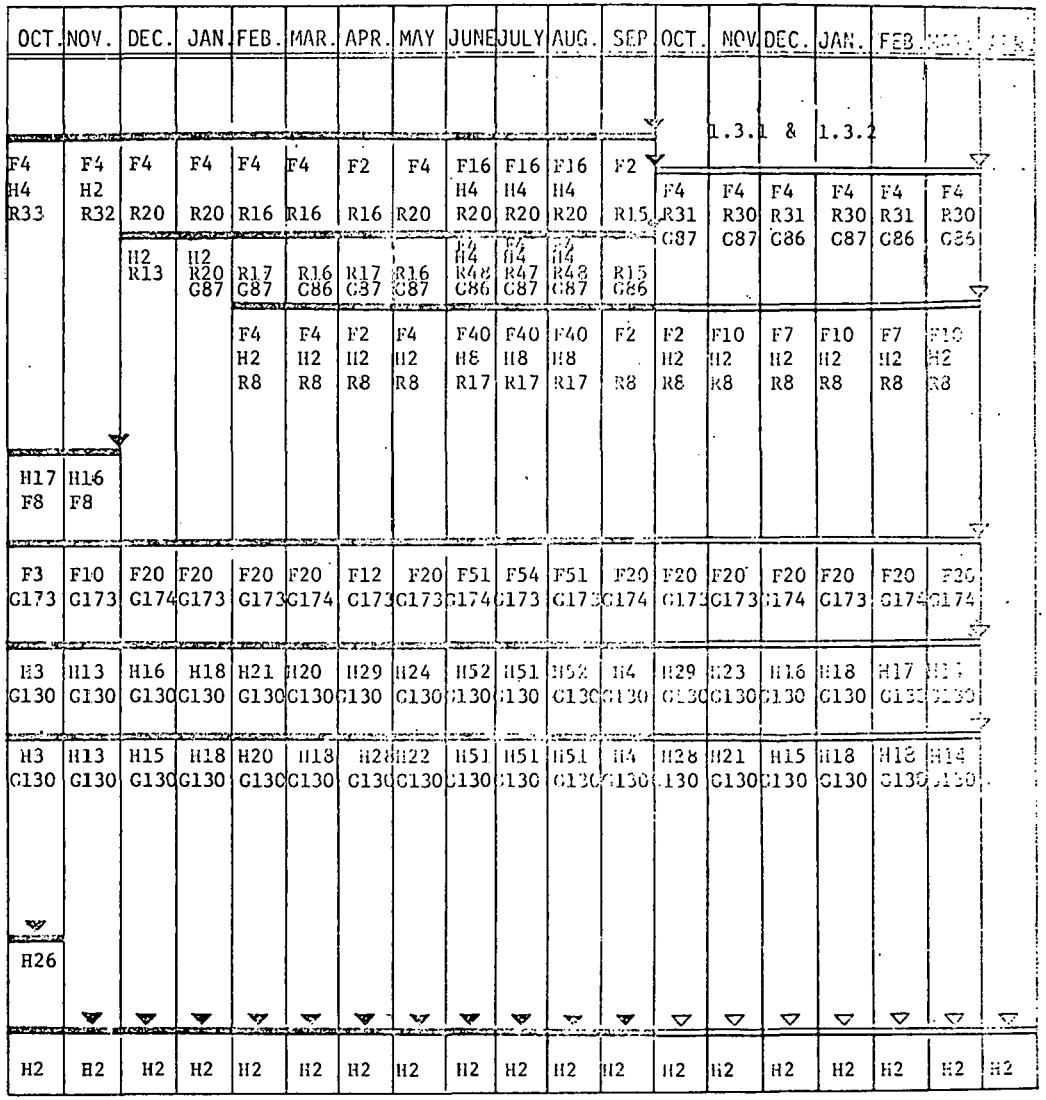

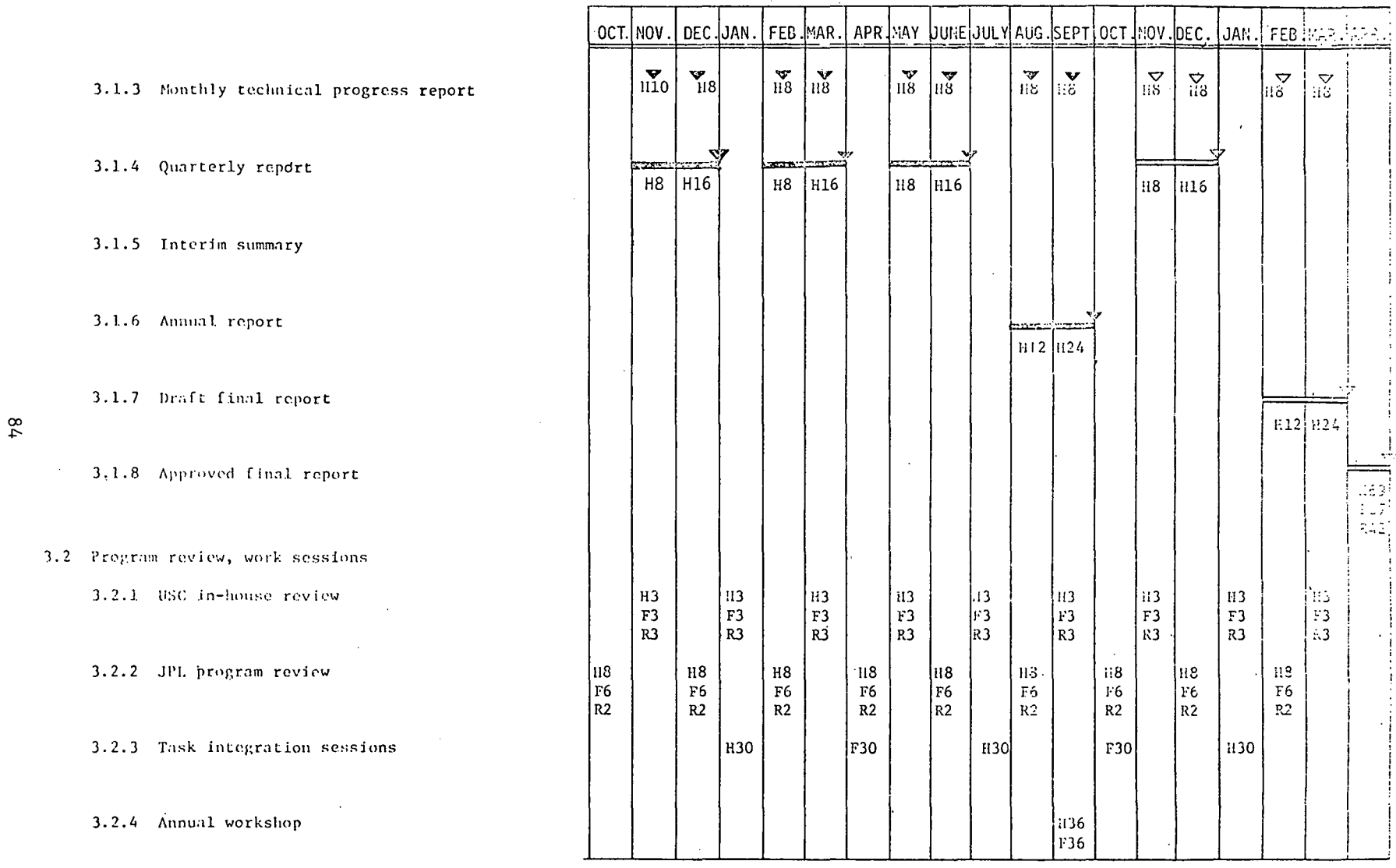
OCT. NOV. DEC. JAN. FEB. MAR. APR. MAY JUNE JULY AUG. SEPT OCT. NOV. DEC. JAN. FEB MAR. APR.
3.1.3 Monthly technical progress report
H10 H8 H8 H8 H8 H8 H8 H8 H8 H8 H8 H8 H8
3.1.4 Quarterly report
H8 H16 H8 H16 H8 H16 H8 H16 H8 H16
3.1.5 Interim summary
3.1.6 Annual report
H12 H24
3.1.7 Draft final report
H12 H24
3.1.8 Approved final report
3.2 Program review, work sessions
3.2.1 USC in-house review
H3 F3 R3 H3 F3 R3 H3 F3 R3 H3 F3 R3 H3 F3 R3 H3 F3 R3 H3 F3 R3 H3 F3 R3 H3 F3 R3 H3 F3 R3
3.2.2 JPL program review
H8 F6 R2 H8 F6 R2 H8 F6 R2 H8 F6 R2 H8 F6 R2 H8 F6 R2 H8 F6 R2 H8 F6 R2 H8 F6 R2 H8 F6 R2
3.2.3 Task integration sessions
H30 F30 H30 F30 H30
3.2.4 Annual workshop
H36 F36

3.2.5 Design and performance review

4. General Administration

5. Planned Cost (Thousands of dollars)

Incurred Cost (Thousands of dollars)